MODELING AND SIMULATION OF SELF-SYNCHRONIZING MECHANICAL SYSTEMS

by

NIKLAS ENDLER

(Under the Direction of R. Benjamin Davis)

ABSTRACT

If certain conditions are met, mechanical systems can exhibit the remarkable ability to self-synchronize. This thesis implements low-order models of two such systems. The first models two coupled pendula attached to a rigid body—a system known as "Huygens' clocks". The two pendula are subject to excitation from an external moment applied by an escapement mechanism. There are two types of escapement models considered: Hamiltonian and Van der Pol. Depending on initial conditions and escapement parameters, the system will fall into one of three post-transient states, which are classified according to the phase difference between the two pendula. These states are in-phase synchronization, out-of-phase synchronization, and asynchronous motion. One objective of this thesis is to map parameter sets and initial conditions to one of these three states. The second model uses principles from the Huygens' clocks model in an adaptation of the well-known "kicked rotor" system. The model consists of two kicked rotors that are coupled via their momenta. The responses of this system indicate rich dynamical behavior, including the possibility of synchronized chaotic motion.

INDEX WORDS: self-synchronization, mechanical oscillators, Huygens' clocks, kicked rotor, synchronized chaos

MODELING AND SIMULATION OF SELF-SYNCHRONIZING MECHANICAL SYSTEMS

by

NIKLAS ENDLER

B.S., The University of Georgia, 2020

A Thesis Submitted to the Graduate Faculty of The University of Georgia in Partial Fulfillment of the Requirements for the Degree

MASTER OF SCIENCE

ATHENS, GEORGIA

2021

© 2021

Niklas Endler

All Rights Reserved

MODELING AND SIMULATION OF SELF-SYNCHRONIZING MECHANICAL SYSTEMS

by

NIKLAS ENDLER

Major Professor: R. Benjamin Davis

Committee: Donald J. Leo
Beshoy Morkos

Electronic Version Approved:

Ron Walcott
Dean of the Graduate School
The University of Georgia
May 2021

Acknowledgements

First, I would like to thank Dr. Davis for his exceptional guidance over the past two years and making this research possible. It has been an absolute pleasure to work under someone so experienced in the field of engineering and dynamics. I would also like to express my appreciation for my committee members, Dr. Leo and Dr. Morkos, for their valuable assessment and advice on my work.

This research has been an extremely challenging, yet rewarding journey. I would like to further thank the UGA College of Engineering for providing me with the tools necessary for completing my research. Lastly, I am deeply grateful for the never-ending support and love from my parents and sister who have helped me get through even the most challenging parts of this thesis. Without them I would not be the person I am today.

Contents

List of Tables

List of Figures

Nomenclature

Greek Symbols

α Constant of motion

δ virtual operator

ϵ Small perturbation constant

Γ Phase space trajectory

γ Gain factor

λ Natural frequency

∇ Gradient

ω Angular frequency

ϕ Phase

θ Angle

θ_{ref} Reference angle

Roman Symbols

ℓ Pendulum length

$\mathbb{R}$ Real numbers

$\mathcal{L}$ Lagrangian

d Pendulum damping

d_3 Rigid body damping

f First integral

I Moment of inertia

J Action variable

K Kicked rotor constant

k_3 Rigid body stiffness

K_c Critical kicked rotor constant

M Connecting rigid body mass

m Pendulum Mass

N Set size

n Time step number

p Momentum

Q Generalized force

q Generalized coordinate

r Radial displacement

T Kinetic energy

T period

t Time

U Potential energy

u External moment / input force

v Radial velocity

W Work

x Linear displacement

$\mathcal{H}^*$ Reference energy

$\mathcal{H}$ Hamiltonian

Super, Subscripts

$\hat{i}, \hat{j}$ Cartesian Vectors

i, k Indices

[,] Poisson bracket

Chapter 1

Introduction and Background

1.1 Synchronization

Self-synchronization is a phenomenon that can sometimes occur in coupled oscillators. Oscillator models are used to predict the behavior of physical systems such as pendula, electric circuits, and planets [1]. The interface between oscillators critically contributes to the feasibility of synchronization. Interest in synchronizing systems has greatly increased over the last century [2], and synchronization is essential to important natural and man-made processes. For example, synchronization is required in power generation and distribution [3], and synchronization of mechanical oscillators has been leveraged in the design of robotic manipulators for assembly lines [4].

Generally, 'to synchronize' means to concur or agree in time, to proceed or to operate at exactly the same rate, to happen at the same time [5, 6]. This definition captures three conventional subdivisions of synchronization [4]:

- In **self-synchronization**, internal system properties enable synchronization between individual oscillators without external influences [4, 5].
- For **controlled-synchronization**, external input or feedback is used to promote synchronization. The U.S. Navy has used controlled synchronization in cryptography for security applications in communications [7].
- In **natural synchronization**, no interconnection between oscillatory systems exists—they act independently, yet can still synchronize. This type of synchronization is relatively rare, but an example given in Ref. [5] which describes clocks synchronizing in the frequency domain.

1.2 Brief History of Self-Synchronization Research

The first documented observation of self-synchronization was made in 1665 by Christiaan Huygens, a Dutch physicist who observed the phenomenon in the movement of pendulum clocks. Huygens played a major role in the scientific revolution and to this day, he is credited with many discoveries in horology, astronomy, and mathematics. Being fascinated by Galileo's previous findings on the pendulum, Huygens spent numerous years combing its principles along with those of mechanical watches. In 1656 he invented the first pendulum clock, which significantly improved time tracking accuracy, from losses of 15 minutes per day to less than 15 seconds [8]. One of Huygens' more famous publications, the *Horologium Oscillatorium*, dives deep into his understanding of oscillatory dynamics in pendulum motion. A big motivator for Huygens' discoveries in horology was solving the longitude problem at sea [9]. One day when Huygens was laying ill in bed, he noticed a strange phenomenon. Two of his pendulum clocks were swinging in opposite directions and at the same frequency (later referred to as out-of-phase synchronization). Over the next few days, Huygens studied this "sympathy" by repeatedly disturbing the clocks to see if they would synchronize. A letter to his father was the first account of this observation. In the letter he mentioned that, within about 30 minutes, the two pendulum clocks hung on the same wooden bar, as seen in Fig. 1.1, would inevitably synchronize out-of-phase [1, 10, 11].

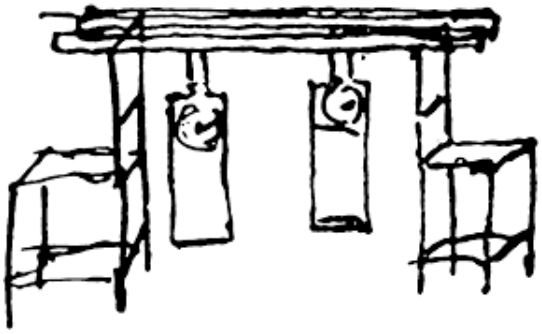

Figure 1.1. Drawing by Huygens from 1665, showing his experimental setup

In 1905, Diederik Korteweg developed the first approach to analytically model Huygens' synchronization using linear theory. Korteweg's approach neglected effects of escapement and damping; however, it provided helpful insight to the modes of the coupled system [2, 10]. Further progress was halted until 1971 when Izrailevich Bleckhman revisited synchronization of dynamic systems. Improving on Kortweg's model, Bleckhman's was the first to consider damped nonlinear oscillations using Van der Pol escapement [12]. Im-

portantly, the findings showed the presence of both an in-phase and out-of-phase post-transient state. In the 1980s, the field of dynamic synchronization experienced more widespread interest [13]. It was during this time that Bleckham further defined self-synchronization and controlled-synchronization [5].

As previously stated, for mechanical systems to synchronize, some type of interface between oscillators must be in place such that motion can be communicated. In the case of Huygens' original synchronization discovery, coupling occurred due to the wooden bar that the pendula to which the pendula were attached [1]. Huygens lacked mathematical concepts of today, including differential calculus, which largely obstructed his quantitative description. However, he noticed the wooden bar come to rest every time the pendula synchronized, therefore attributing synchronization as a byproduct of the bar's motion [1, 2, 11]. Over recent years a variety of experiments replicated Huygens' setup, one of which was performed by Bennett et al. [14]. They considered the ratio between the masses of the pendula and that of the connecting body, and recognized that as this mass ratio increases, the probability of out-of-phase synchronization goes down. A common alternative adaptation of the Huygens model has been the substitution of metronomes for the pendula. Ref. [15] discusses such a case. The findings show consistent in-phase synchronization compared to the out-of-phase synchronization that occurs with pendula. In Ref. [15], the difference is attributed to the larger frequency variance in the metronomes and lower coupling mass.

Coupled pendula and metronomes exhibit periodic self-synchronization. Amazingly, synchronized non-periodic (i.e., chaotic) behavior is also possible. Applications for chaotic synchronization have been found in the field of cryptography chaotic signals are used to encrypt communications signals, and synchronized chaos is used in the decryption [16, 17].

1.3 Contributions of Thesis

The goal of this thesis is to implement numerical models of self-synchronizing systems in an effort to better understand this fascinating phenomenon. Chapter 2 implements a previously studied Huygens' clocks model, and uses it to generate some new results. Chapter 3 presents a novel duel kicked-rotor model that can exhibit synchronized chaos.

The list below summarizes the main contributions of this thesis:

- An independent implementation of a Huygens' clocks model is created and exercised across a large configuration space.
- Several initial condition maps are generated for the Huygens' clocks model. Such maps are rarely found in the literature.
- A study of the linearized natural modes of the Huygens' clocks model provides insight into how the center mass behaves in the different synchronized states.
- Introduction of natural frequency variation in Huygens' clocks model generates numerical results that are in agreement with experimental observations
- Formulation and analysis of novel model constituting of two kicked rotors. The system is shown to exhibit both synchronous and asynchronous periodic and chaotic motion.
- The initial conditions leading to each type of motion in the dual kicked rotor system are mapped to show a complicated dependence on initial conditions.
- Due to its relative simplicity, this new kicked rotor model is thought to have applications to Physics education. It could also help explain perplexing phenomena from quantum mechanics.

Chapter 2

Numerical Model of Huygens' Clocks

2.1 Description

This chapter covers the modeling of a mechanical system exhibiting synchronization. The model is inspired by Huygens' synchronizing clocks, as described in Chapter 1. The model consists of two damped, identical pendula connected through a common, elastically restrained and damped mass (see Fig. 2.1). An escapement mechanism is modeled such that it provides a moment to each pendulum depending on its angular position. The system is modeled and then solved numerically using Matlab's ode45 integrator, i.e. the Runge-Kutta funciton, to investigate the configurations leading to synchronization.

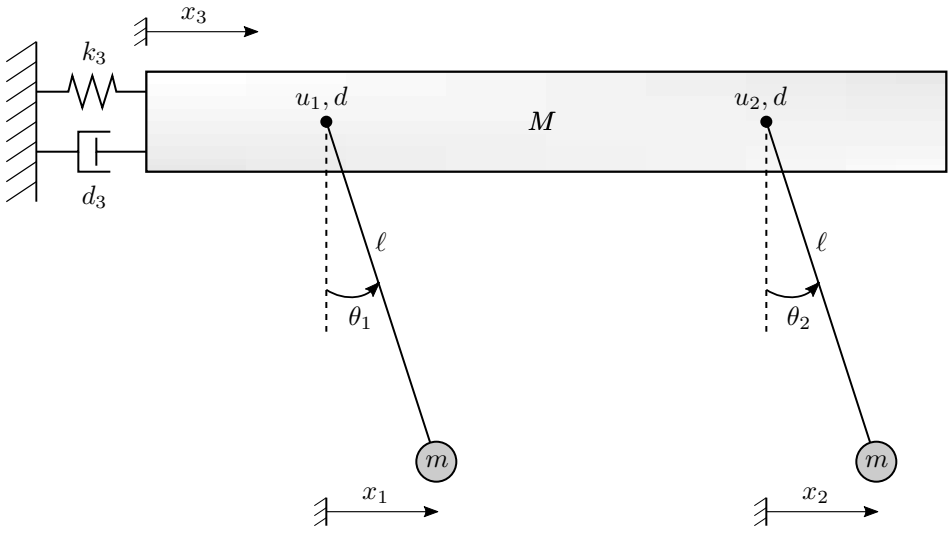

Figure 2.1. Schematic of the Huygens' clocks model

2.2 Equations of Motion

The equations of motion for the three degree-of-freedom system shown in Fig. 2.1 are derived using Lagrange's equation of motion, which can be written in terms of the Lagrangian, i.e.,

$$\mathcal{L} = T - U, \tag{2.1}$$

where T and U are the total kinetic and potential energies of the system. In terms of T and U, Lagrange's equations of motion are

$$\begin{aligned} \frac{d}{dt}\left(\frac{\partial T}{\partial \dot{q}_k}\right) - \frac{\partial T}{\partial q_k} + \frac{\partial U}{\partial q_k} &= Q_k, \\ \delta W = \sum_{k=1}^{n} Q_k \delta q_k, \quad k &= 1, 2, ...N. \end{aligned} \tag{2.2}$$

Here, q_k are the generalized coordinates. In the present model, the generalized coordinates are θ_1, θ_2, and x_3. The generalized forces are given by Q_k, and are expressed in terms of the virtual work, δW, acting over a virtual displacement, δq_k.

The kinetic energy of the system can be found by adding the kinetic energies of the center mass and the pendula

$$T = \frac{1}{2} M \dot{x}_3^2 + \sum_{i=1}^{2} \left(\frac{1}{2} m \vec{v}_i \cdot \vec{v}_i\right). \tag{2.3}$$

Next, the velocities of the pendula are found by writing their position vectors, i.e., $\vec{r_i} = (\ell \sin\theta_i + x_3)\hat{i} - (\ell\cos\theta_i)\hat{j}$ and $\vec{v_i} = \dot{\vec{r_i}} = (\ell\dot{\theta}_i\cos\theta_i + \dot{x}_3)\hat{i} + (\ell\dot{\theta}_i\sin\theta_i)\hat{j}$ for i=1, 2. The dot product of the velocity vectors is then

$$\vec{v}_i \cdot \vec{v}_i = (\ell\dot{\theta}_i\cos\theta_i + \dot{x}_3)^2 + (\ell\dot{\theta}_i\sin\theta_i)^2 = \dot{x}_3^2 + 2\ell\dot{x}_3\dot{\theta}_i\cos\theta_i + \ell^2\dot{\theta}_i^2 \quad i = 1, 2. \tag{2.4}$$

Substituting Eq. (2.4) into Eq. (2.3) and simplifying then yields the system's total kinetic energy

$$T = \frac{1}{2}(M + 2m)\dot{x}_3^2 + \sum_{i=1}^{2}\left(m\ell\dot{x}_3\theta_i\cos\theta_i + \frac{1}{2}m\ell^2\dot{\theta}_i^2\right). \tag{2.5}$$

The potential energy of the system is simply given by the elastic potential energy of the spring, plus the potential energy from the change in height of the pendula,

$$U = \frac{1}{2}kx_3^2 + \sum_{i=1}^{2}(mg\ell(1 - \cos\theta_i)). \tag{2.6}$$

The individual terms in Lagrange's equation, Eq. (2.2), with respect to x_3 are

$$\begin{aligned}
\frac{d}{dt}\left(\frac{\partial T}{\partial \dot{x}_3}\right) &= \frac{d}{dt}\left((M+2m)\dot{x}_3 + \sum_{i=1}^{2}(m\ell\dot{\theta}_i\cos\theta_i)\right), \\
&= (M+2m)\ddot{x}_3 + \sum_{i=1}^{2}(m\ell\ddot{\theta}_i\cos\theta_i - m\ell\dot{\theta}_i^2\sin\theta_i), \\
-\frac{\partial T}{\partial x_3} &= 0, \\
\frac{\partial U}{\partial x_3} &= k_3 x_3, \\
Q_{x_3} &= d_3\dot{x}_3,
\end{aligned} \tag{2.7}$$

which lead to the equation of motion for the center mass

$$(M+2m)\ddot{x}_3 + k_3 x_3 + d_3\dot{x}_3 + \sum_{i=1}^{2}(m\ell\ddot{\theta}_i\cos\theta_i - m\ell\dot{\theta}_i^2\sin\theta_i) = 0. \tag{2.8}$$

The individual terms of Lagrange's equation with respect to θ_i for $i = 1, 2$ are

$$\begin{aligned}
\frac{d}{dt}\left(\frac{\partial T}{\partial \dot{\theta}_i}\right) &= \frac{d}{dt}\left(m\dot{x}_3\ell\cos\theta_i + m\ell^2\dot{\theta}_i\right), \\
&= m\ddot{x}_3\ell\cos\theta_i - m\dot{x}_3\ell\dot{\theta}_i\sin\theta_i + m\ell^2\ddot{\theta}_i, \\
-\frac{\partial T}{\partial \theta_i} &= m\dot{x}_3\ell\dot{\theta}_i\sin\theta_i, \\
\frac{\partial U}{\partial \theta_i} &= mg\ell\sin\theta_i, \\
Q_{\theta_i} &= -d\theta_i.
\end{aligned} \tag{2.9}$$

The final equation of motion for the pendula are then

$$m\ell^2\ddot{\theta}_i + d\dot{\theta}_i + mg\ell\sin\theta_i + m\ell\ddot{x}_3\cos\theta_i = u_i, \quad i = 1, 2. \tag{2.10}$$

Here $u_i(t)$ represents an external moment provided by the escapement mechanism.

2.3 Escapement

Escapement is the transfer of stored energy—usually in the form of a spring or suspended mass—to the gears of a clock in order to overcome frictional forces [18]. This energy addition heavily determines the accuracy of a clock. For example, the escape fork in a wristwatch often oscillates two or three times a second [18]. One can imagine that if such oscillation is off by just one hundredth of a second, over a

full day (86,400 seconds), the effect becomes significantly magnified. Even though uncommon due to complexity, one error mitigation approach has been to purposely introduce coupled resonance in watches. Through coupled resonance, the periodic motion of multiple escapements can be averaged, such as in the 2005 Haldimann H2 Flying Resonance. Here, a coupling spring links the arbors of two fly wheels (in gold) to average out imperfections in the hairspring's oscillations, see Fig. 2.2 [18, 19]. This is not unlike the way in which the two pendula are coupled in the Hygens' clocks model.

Figure 2.2. Image of Haldimann H2 Flying Resonance watch. Notice the thin coupling spring connecting the two individual escapement mechanisms on each side.

In the Huygens' clock model, damping of the bar and pendula causes the system to lose energy, so the motion will eventually decay to zero without an escapement mechanism. One such escapement model is known as Hamiltonian escapement. The Hamiltonian is often defined as the total energy in the system, i.e.,

$$\mathcal{H} = T + U. \tag{2.11}$$

Using the Hamiltonian as in Refs. [20–23] provides a means of determining the external moment, $u(t)$, that is applied to the pendula. For the pendula, the Hamiltonian is given by

$$\mathcal{H}_i(\theta_i, \dot{\theta}_i) = \frac{m\ell^2\dot{\theta}_i^2}{2} + mg\ell(1 - \cos\theta_i), \quad i = 1, 2. \tag{2.12}$$

One can find the reference energy, $\mathcal{H}^*$, to reach a certain angle, θ_{ref}, by focusing on potential energy at the desired amplitude, with the kinetic energy equal to zero, i.e.,

$$\mathcal{H}_i^* = mg\ell(1 - \cos\theta_{\text{ref}}). \tag{2.13}$$

Using a nonlinear feedback control method called the *speed gradient*, the appropriate input control function, $u(t)$, is formulated such that the desired $\mathcal{H}^*$ is achieved [5, 20, 22, 24–26],

$$u_i = -\gamma(\mathcal{H}_i - \mathcal{H}^*)\dot{\theta}_i, \quad i = 1, 2. \tag{2.14}$$

Upon substitution, this gives

$$u_i = -\gamma\left(\frac{m\ell^2\dot{\theta}_i^2}{2} + mg\ell(\cos\theta_{\text{ref}} - \cos\theta_i)\right)\dot{\theta}_i, \quad i = 1, 2. \tag{2.15}$$

Accounting for Hamiltonian escapement, the equations of motion for the pendula are now

$$m\ell^2\ddot{\theta}_i + \left(d + \gamma\left(\frac{m\ell^2\dot{\theta}_i^2}{2} + mg\ell(\cos\theta_{\text{ref}} - \cos\theta_i)\right)\right)\dot{\theta}_i + mg\ell\sin\theta_i + m\ell\cos\theta_i\ddot{x}_3 = 0, \quad i = 1, 2. \tag{2.16}$$

Dividing both sides of Eq. (2.16) by $m\ell^2$ yields

$$\ddot{\theta}_i + \left(\frac{d}{m\ell^2} + \gamma\left(\frac{\dot{\theta}_i^2}{2} + \frac{g}{\ell}(\cos\theta_{\text{ref}} - \cos\theta_i)\right)\right)\dot{\theta}_i + \frac{g}{\ell}\sin\theta_i + \frac{1}{\ell}\cos\theta_i\ddot{x}_3 = 0, \quad i = 1, 2. \tag{2.17}$$

At this point, we define $\omega^2 = g/\ell$ and $\beta = d/(m\ell^2\gamma)$ such that

$$\ddot{\theta}_i + \gamma\left(\beta + \frac{\dot{\theta}_i^2}{2} + \omega^2(\cos\theta_{\text{ref}} - \cos\theta_i)\right)\dot{\theta}_i + \omega^2\sin\theta_i + \frac{\omega^2}{g}\ddot{x}_3\cos\theta = 0, \quad i = 1, 2. \tag{2.18}$$

Turning attention to the center mass, we can further reduce the number of input parameters in the system by treating the center mass as a rigid body (i.e., neglect its stiffness and damping). This simplifies Eq. (2.8) to

$$\ddot{x} + \sigma\sum\left(\ddot{\theta}_i\cos\theta_i - \dot{\theta}_i^2\sin\theta_i\right) = 0, \quad i = 1, 2, \tag{2.19}$$

where $\sigma = m\ell/(M + 2m)$. At this point, the total number of parameters needing to be declared is reduced to six: γ, β, g, ω, θ_{ref}, and σ. Ways of further simplifying the equations of motion do exist such as in Ref. [2], however, they necessitate some approximations.

Note that Hamiltonian escapement is just one of many possible types of escapement models. But unlike other models, Hamiltonian escapement resides on a continuous nonlinear function which maintains the smoothness of the system [10]. The time-varying inputs, θ and $\dot{\theta}$, continuously adjust the escapement to the reference energy, $\mathcal{H}^*$. In a realistic clock mechanics, however, escapement supplies impulses of energy into the system to maintain its amplitude [14].

Fig. 2.3 shows how the Hamiltonian escapement input changes according to θ and $\dot{\theta}$ for a reference angle of 0.35 rad. The largest inputs for u correspond to positive and negative extremes of angular velocity, $\dot{\theta}$, and θ. Note that a negative value of u corresponds to an increase in system energy.

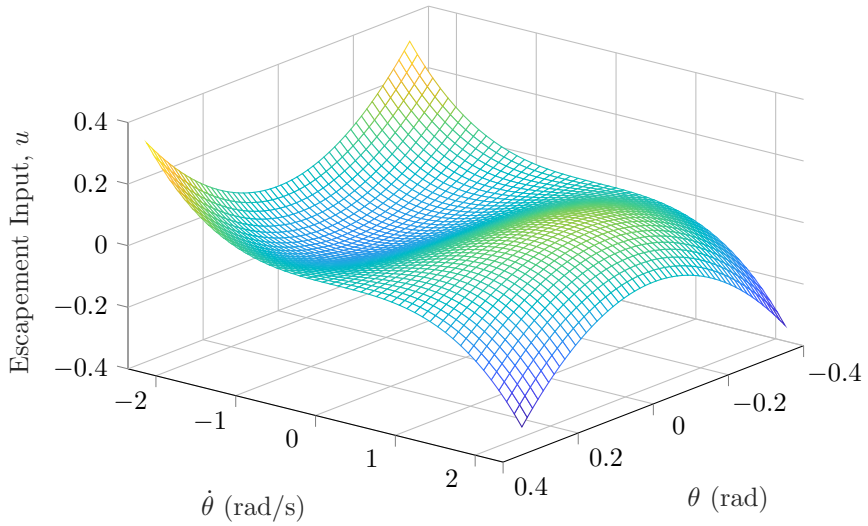

Figure 2.3. The Hamiltonian escapement input, u, over angles of -0.35 to 0.35 rad and rotational velocities of -2.35 to 2.35 rad/s with $\gamma = 1$ and $\theta_{\text{ref}} = 0.35$ rad.

The equations of motion of the system can now be solved with numerical integration. After an initial transient, the pendula are expected to assume one of three states: (1) in-phase synchronization, (2) out-of-phase synchronization, (3) or asynchronous motion. In-phase synchronization indicates that $\phi_1(t) = \phi_2(t)$, where ϕ denotes the phase of each pendulum. Out-of-phase synchronization is defined by $|\phi_1(t) - \phi_2(t)| = \pi$. If neither of these two states are determined at the end of some transient, the system is said to be asynchronous.

To define synchronization for the sake of the numerical model, a certain tolerance must be implemented. For all simulations used here, if the pendula are said to be in-phase if they have a phase difference of less than one-hundredth of a degree at steady state. Similarly, if the pendula have a phase difference of $\pi \pm 0.01°$, they are categorized as out-of-phase.

2.4 Verification

To verify the implementation of the numerical model, results from Ref. [1] are reproduced. Here, the input parameters are: $m = 1$ kg, $M = 50$ kg, $d = 0.01$ Nms/rad, $d_3 = 20$ Ns/m, $k_3 = 1$ N/m, $g = 9.81$

m/s^2, $l = 0.2184$ m, $\dot{\theta}_1(0) = \dot{\theta}_2(0) = x(0) = \dot{x}(0) = 0$, and $\theta_{\text{ref}} = 0.35$ rad. Figs. 2.4 and 2.5 each show the same four sub-plots, where Fig. 2.4 comes from Ref. [1] and Fig. 2.5 is from the present implementation.

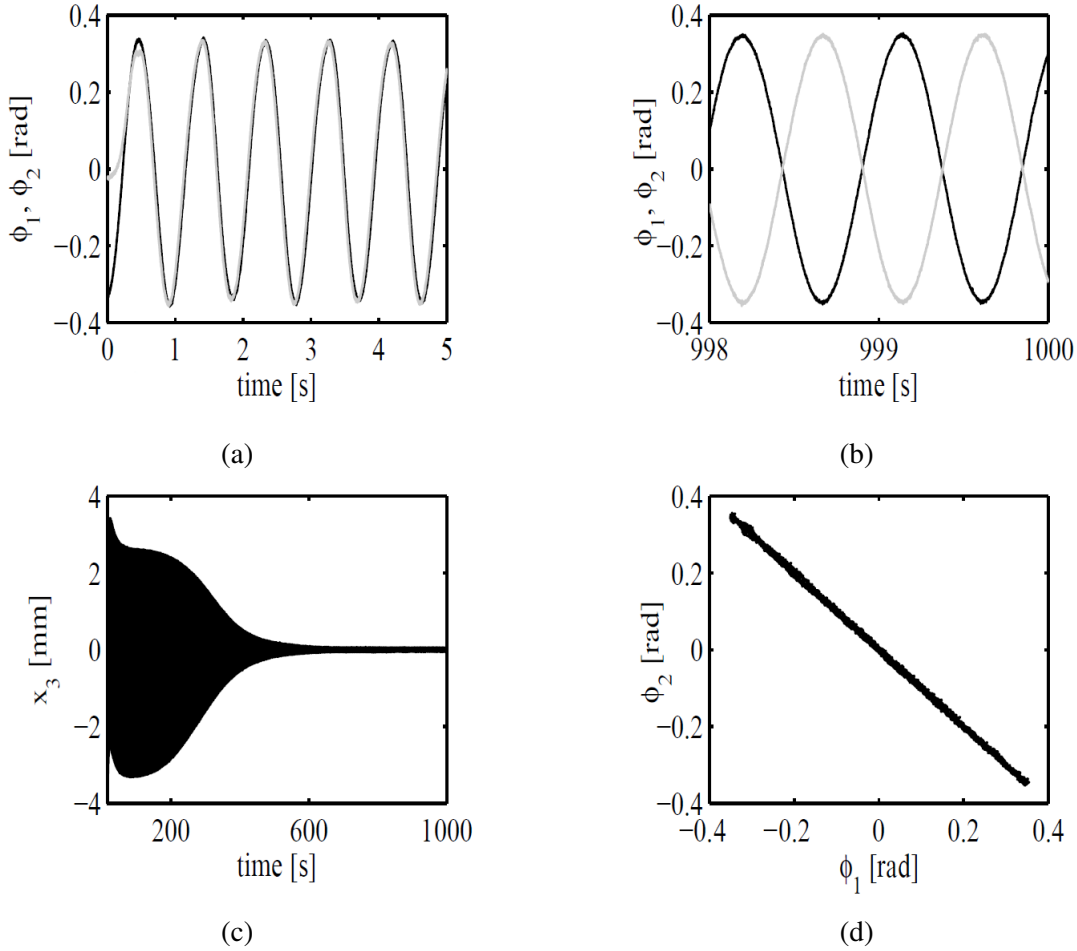

Figure 2.4. Figures reproduced from Ref. [1] showing the beginning of the time history for the pendula before synchronization (top left), the same time history after synchronization has occurred (top right), the time history of the rigid mass (bottom left), and angles of the two pendula plotted against each other over time (bottom right). Here, $\gamma = 5.3$, $\phi_1(0) = -0.32$ rad and $\phi_2(0) = -0.02$ rad. Note that in Ref. [1], ϕ is used to represent the angular position of the pendula.

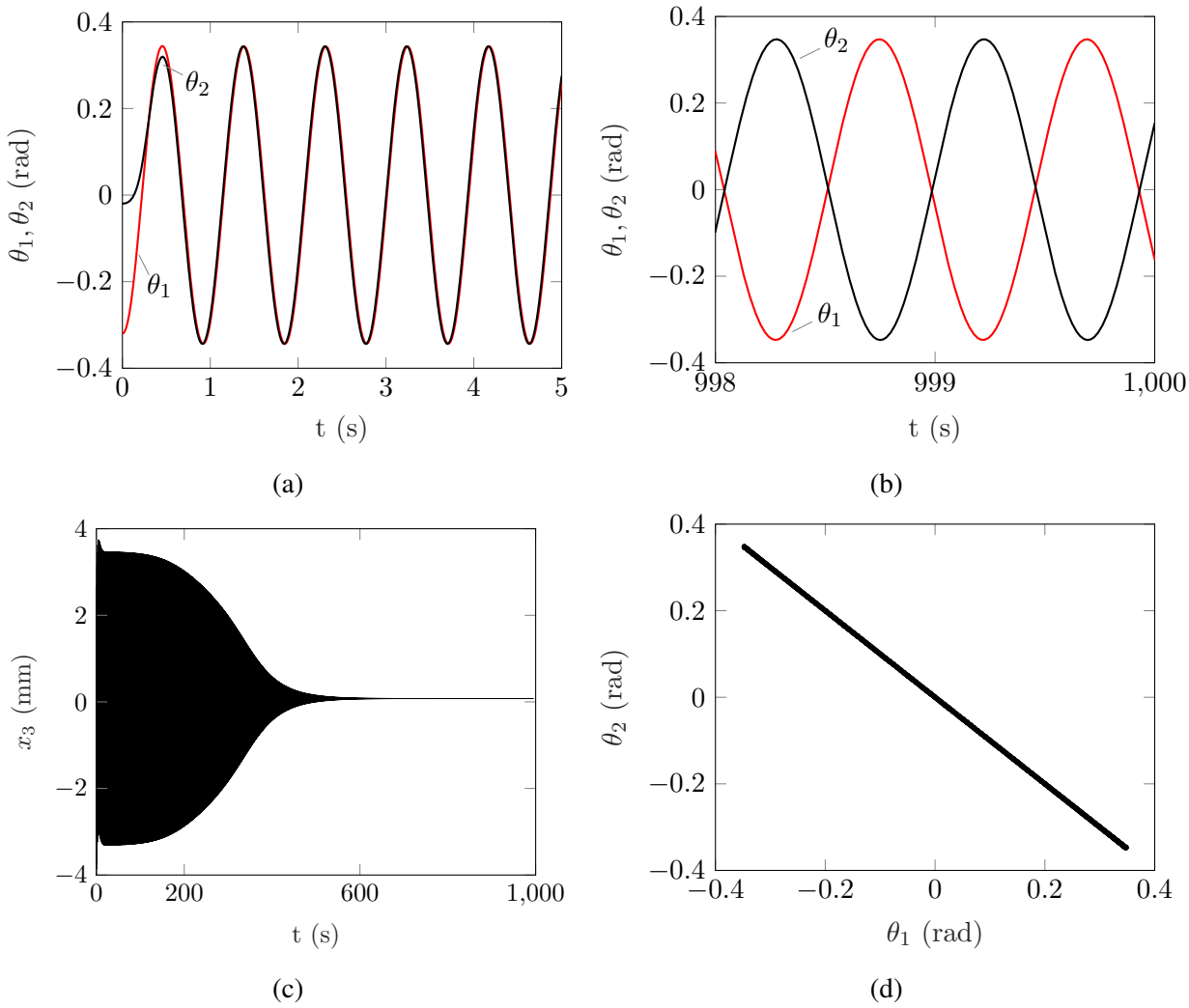

Figure 2.5. Reproduction of results from Ref. [1] as produced by the present model implementation. Again, $\gamma = 5.3$, $\theta_1(0) = -0.32$ rad and $\theta_2(0) = -0.02$ rad.

2.5 Initial Conditions

Nonlinear dynamical systems can exhibit sensitivity to initial conditions. This section considers how the initial conditions of the Huygens' clock model influence whether the model exhibits self-synchronization. To generate the initial condition maps shown in Fig. 2.7, the starting angles of the pendula, θ_{1_0} and θ_{2_0}, are varied between -0.5 and 0.5 rad with the escapement scalar, γ, fixed. A total of 10,201 (101 $\times$ 101) different angles combinations are considered in each map. In each case, synchronization is classified after 5,000 seconds of simulated response.

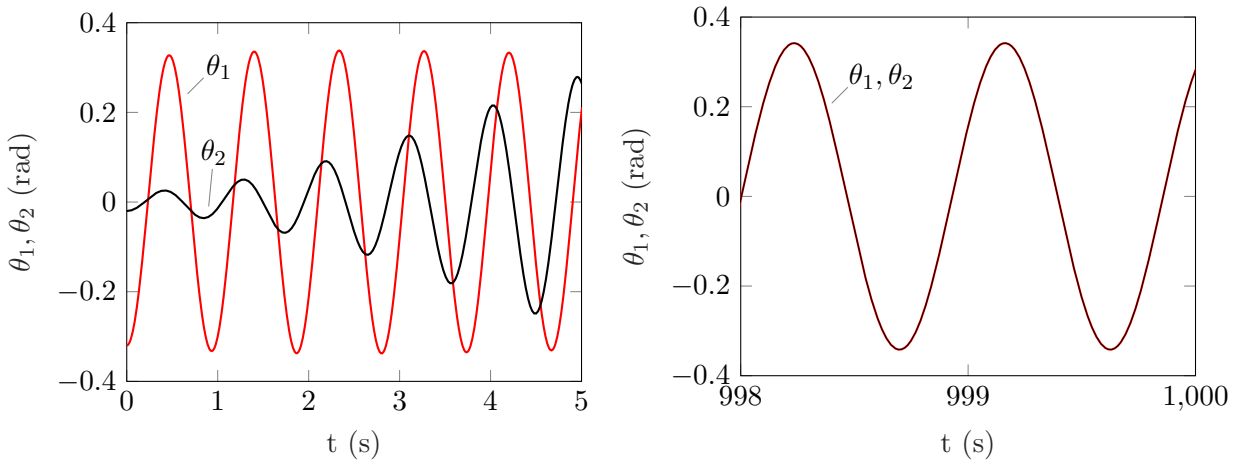

Figure 2.6. Time histories for $\phi_1(0) = -0.32, \phi_2(0) = -0.02, \gamma = 0.3$. All other system parameters are consistent with those given in the beginning of Sec. 2.4.

The initial condition maps show that the system is more prone to synchronize in-phase (blue) when the two pendula are released with near-identical angles. However, when the initial angle combinations involve a difference of sign, the system tends to synchronize out-of-phase (red). Note that when the escapement gain factor, γ, is increased, the pendula are more likely to synchronize out-of-phase. It is also noted that depending on the initial conditions, the time it takes the system to reach steady-state varies.

The present model may be categorized as asymptotic, meaning it will only synchronize under certain initial conditions and with certain escapement parameters [5, 26]. As observed in Refs. [10, 14, 15], the coupling strength relies on the mass ratio, m/M, between the individual pendula, m, and the center mass, M. This correlation can be seen in Fig. 2.8. As the mass of the center block increases from 1 to 100 kg (or the mass ratio decreases from 1 to 0.010 with $m = 1$ kg), the time required to reach a synchronous state goes up. In the case of $\gamma = 0.4$, it seems to go up linearly for $M > 16$ kg while for $\gamma = 4.0$, the curve appears exponential.

With $\gamma = 4.0$, out-of-phase synchronization is reached for all considered mass ratios. Whereas with $\gamma = 0.4$, the local peak at $M = 7.9$ kg corresponds to a transition from an out-of-phase synchronous state to in-phase synchronous state. Transitioning behavior has been supported experimentally [1], where it was observed that experimental setups with smaller m/M ratios, result in out-of-phase synchronization while systems with higher mass ratios tend to synchronize in-phase. As described in Ref. [1, 15], varying the

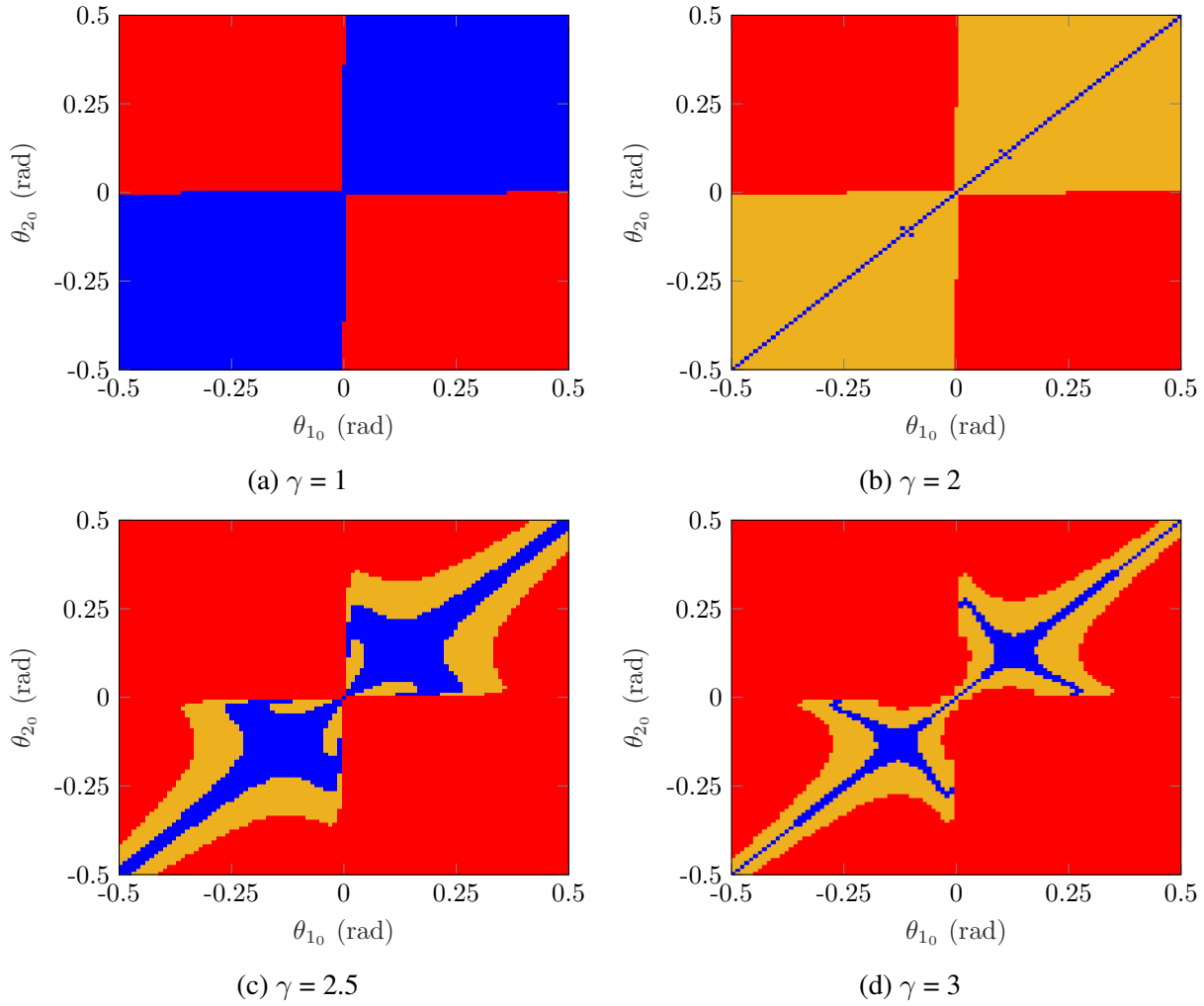

(a) γ = 1

(b) γ = 2

(c) γ = 2.5

(d) γ = 3

Figure 2.7. Initial condition maps for select values of γ. Blue, red, and yellow indicate in-phase synchronization, out-of-phase synchronization asynchronous behavior, respectively. For simplicity $d = 0$ Nms/rad, all other system parameters are consistent with those given in the beginning of Sec. 2.4.

weight of the connecting mass of two, coupled metronomes dictated the type of synchronization. It also seems that Christiaan Huygens observed out-of-phase synchronization in all of his results. As described in Refs. [11, 15], the base that he used to connect the pendula in Huygens' experimental setup was extremely massive, which is consistent with the present trend. However, it is also noted that the escapement gain factor, γ, also plays a role in determining the final synchronized state.

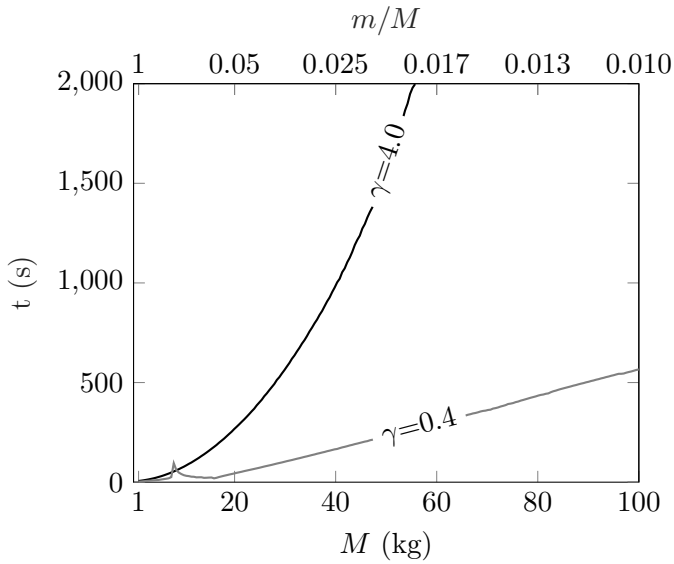

Figure 2.8. Correlation of coupling strength — both individually looking at the center block mass, M, and mass ratio between the pendula and the center block, m/M — to synchronization time for $\gamma = 0.4$ (grey) and $\gamma = 4.0$ (black) given initial angles 0.1 (rad) and 0.2 (rad) for pendulum 1 and pendulum 2 respectively.

2.6 Modes

In an attempt to better understand the behavior of the Huygens' clocks model, this section considers the model's linearized natural modes. The linearized equations of motion of the pendula and the center mass are

$$m\ell^2\ddot{\theta}_i + d\dot{\theta}_i + mg\ell\theta_i + m\ell\ddot{x}_3 = 0, \quad i = 1, 2, \tag{2.20}$$

$$(M + 2m)\ddot{x}_3 + d_3\dot{x}_3 + k_3x_3 + \sum_{i=1}^{2}(m\ell\ddot{\theta}_i) = 0. \tag{2.21}$$

Here, a small angle approximation was applied and nonlinear terms were neglected. In matrix-vector form, the equations of motion are

$$\underbrace{\begin{bmatrix} m\ell^2 & 0 & m\ell \\ 0 & m\ell^2 & m\ell \\ m\ell & m\ell & M+2m \end{bmatrix}}_{\text{[M]}} \begin{Bmatrix} \ddot{\theta}_1 \\ \ddot{\theta}_2 \\ \ddot{x}_3 \end{Bmatrix} + \underbrace{\begin{bmatrix} d & 0 & 0 \\ 0 & d & 0 \\ 0 & 0 & d_3 \end{bmatrix}}_{\text{[C]}} \begin{Bmatrix} \dot{\theta}_1 \\ \dot{\theta}_2 \\ \dot{x}_3 \end{Bmatrix} + \underbrace{\begin{bmatrix} mg\ell & 0 & 0 \\ 0 & mg\ell & 0 \\ 0 & 0 & k_3 \end{bmatrix}}_{\text{[K]}} \begin{Bmatrix} \theta_1 \\ \theta_2 \\ x_3 \end{Bmatrix} = \begin{Bmatrix} 0 \\ 0 \\ 0 \end{Bmatrix}. \tag{2.22}$$

The natural modes of the system are given below, in Table 2.1.

Mode Shapes			
Mode and Wavelength	Mode 1 ($\lambda = 0.022$ Hz)	Mode 2 $\lambda = 1.067$ Hz)	Mode 3 ($\lambda = 1.088$ Hz)
Pendulum 1	0.002	1.000	1.000
Pendulum 2	0.002	-1.000	1.000
Center Mass	1.000	0.000	-0.008

Table 2.1. System Modes and Wavelengths.

Mode 1 is heavily dominated by the motion of the center mass. In Mode 2, the pendula are out-of-phase, and in-phase in Mode 3. Note that in Modes 1 and Mode 3, in-phase motion of the pendula corresponds to non-zero motion of center mass. When the system synchronizes out-of-phase, however, the forces from the pendula cancel each other out, and the center mass moves back to its equilibrium position. Therefore, the motion of the center mass can be used to classify whether the system is synchronized in-phase or out-of-phase.

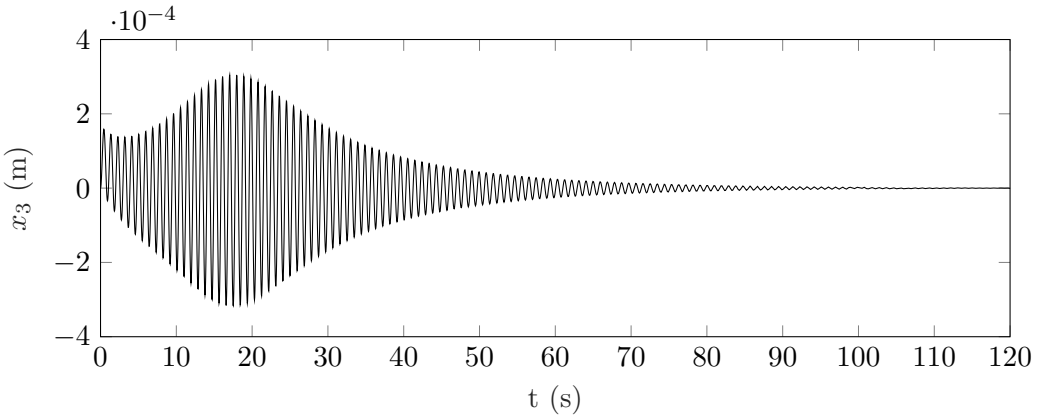

Figure 2.9. Time history for the center mass given $\theta_{1_0} = 0.05$, $\theta_{2_0} = -0.03$, $\gamma = 0.2$, and parameters given in Sec. 2.4.

Fig. 2.9 shows a representative motion of the center mass. At 18 seconds, the pendula nearly synchronize in-phase, which is marked by an increase in center mass displacement. However, the motion of the center mass then settles down, indicated the final state is out-of-phase synchronization. Fig. 2.10, shows how amplitude of the motion the center mass changes with initial conditions. The results are consistent with the initial condition maps shown in Fig. 2.7a. Namely, the bar has high amplitudes in the first and third

quadrants, which corresponds to in-phase motion of the pendula, while in the second and fourth quadrants, the bar's motion is minimal, indicating out-of-phase synchronization.

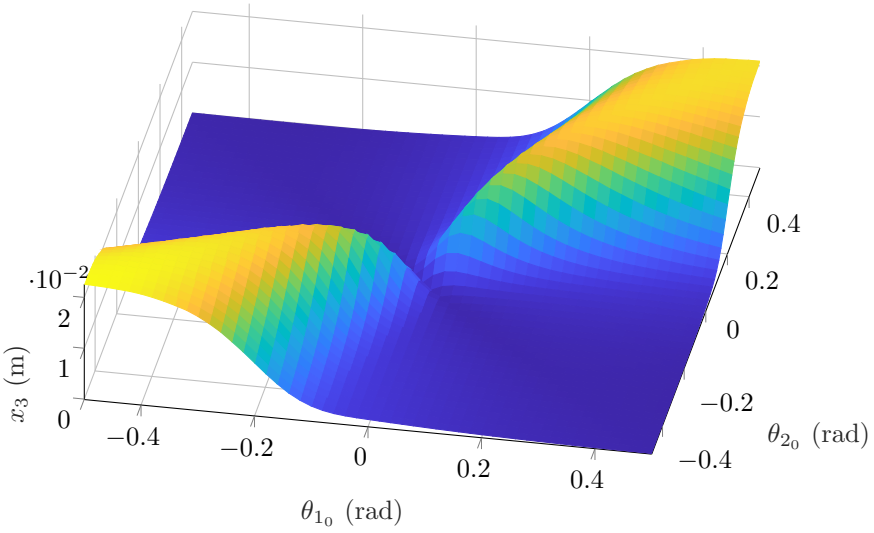

Figure 2.10. Variance in center mass displacement for initial angles, θ_1 and θ_2, -0.5 to 0.5 (rad), $\gamma = 0.5$ after 100 second. Initial conditions are given in Section 2.4 with the exception that $M = 10$ (kg) and $l = 1$ (m) for amplification in center mass displacement.

2.7 Pendula with Different Natural Frequencies

In a physical implementation of Huygens' clock experiment, a slight difference in the linearized natural frequency of the two pendula is expected. Altering the natural frequency of a simple pendulum, $\sqrt{g/l}$, can then be done by means of varying gravity or length. Since gravity on both pendula is the same in a typical physical situation, the natural frequency of a pendulum is varied by adjusting its length. To determine an appropriate amount of variation to apply to the pendulum length, Ref. [14] was consulted. This reference claims that at the time of Huygens's discovery pendulum clocks were able to record time within 15 seconds of each day. With two pendula, this corresponds to a maximum possible time difference of 30 seconds a day. A 0.069% difference in natural could account for such a shift.

Fig. 2.11 shows two initial condition maps in which there is this small difference in natural frequencies of the two pendula. For the low mass ratio case, Fig. 2.11a, no angle combinations (excluding the trivial $\theta_{1_0} = \theta_{2_0} = 0$ combination) resulted in synchronization. It has also been remarked experimentally that altering the natural frequencies beyond a certain threshold ceased synchronization all together [15]. On the

contrary, as can been seen in Fig. 2.11a, maintaining all other parameters the same and only reducing the coupling strength, m/M, causes all angle combinations to synchronize out-of-phase. Even initial conditions where $\theta_{1_0} = \theta_{2_0}$ synchronized out-of-phase. These results support Huygens's observations in 1665. His findings only mention out-of-phase synchronization [11].

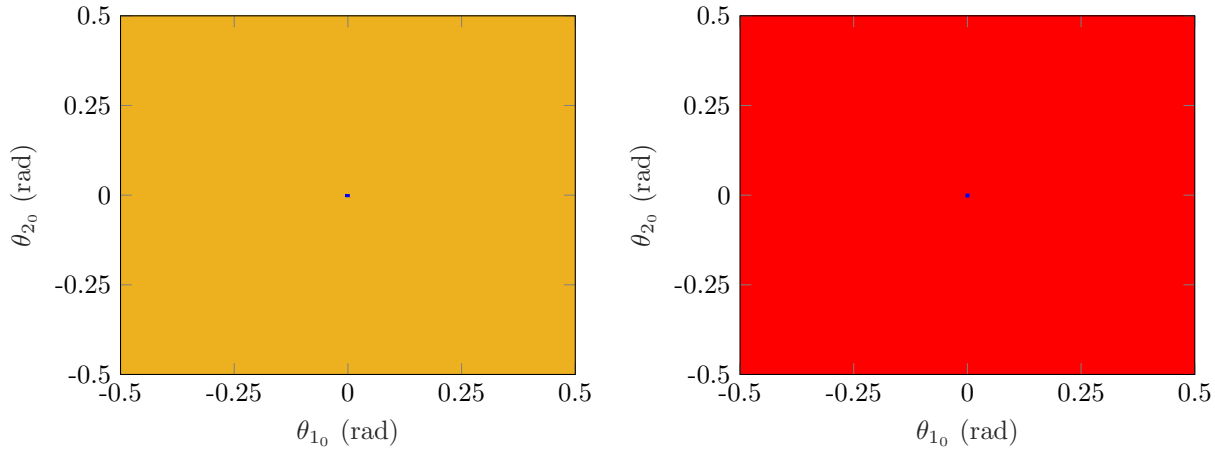

(a) m/M = 1/50 (b) m/M = 1/3

Figure 2.11. Shows the affect of alterning the natural frequencies between the pendula by 0.069% for (a) $m/M = 1/50$ and (b) $m/M = 1/3$ while $\gamma = 1$. Apart from these adjustments, the same initial conditions as in Sec. 2.4 held true.

2.8 Van der Pol Escapement

One of the simplest types of non-linear, self-exciting models is the Van der Pol oscillator [2]. In this model, non-linearity enters the system in the damping term. Here, instead of a Hamiltonian escapement mechanism, a van der Pol escapement is considered, where the external torque is given by

$$u_i = \gamma(\theta_{\text{ref}}^2 - \theta_i^2)\dot{\theta}_i, \quad i = 1, 2. \tag{2.23}$$

As indicated above, only the difference of the squares of the pendulum's angle and the reference angle dictate the applied torque. This term adds energy for angles below θ_{ref}, and deducts energy for larger angles. Van der Pol escapement has been used to model synchronization in metronomes and carts [1, 2].

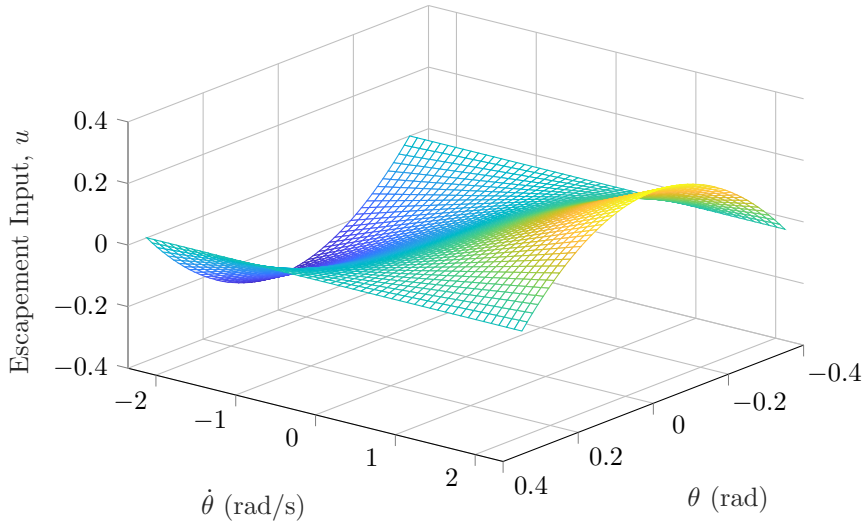

Figure 2.12. Shows the Van der Pol escapement input, u, over angles of -0.35 to 0.35 rad and rotational velocities of -2.35 to 2.35 rad/s. Again, the range on the axes for θ and $\dot{\theta}$ was chosen to encompass all state values when the reference angles is set to 0.35 rad.

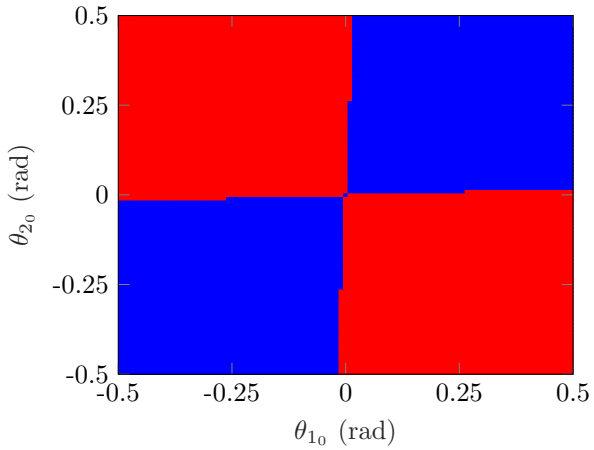

Figure 2.13. Initial condition map, with the same system initial conditions as in Fig. 2.7a(a) with the exception that θ_{ref} = 0.1 rad. Again, blue indicates in-phase synchronization and red indicates out-of-phase synchronization.

To better compare the response of the model using the Van der Pol escapement to the model using Hamiltonian escapement, the exact same initial conditions were used. Based on Fig. 2.12 and Fig. 2.13, the two escapements do influence the system in a very similar way. Specifically when comparing Fig. 2.7a to Fig. 2.13, one can see they are almost identical. Where the figures do vary is along the zero axes. However, with that exception, in both cases the pendula almost always synchronize in-phase and out-of-phase based on the phase difference of their initial angles.

2.9 Summary

This chapter implements a mechanical oscillator model of Huygens' clocks. It is one of the rare studies to use initial condition maps to track system behavior across different initial conditions and escapement gains. With both Hamiltonian and Van der Pol escapement, the initial conditions play a crucial role in determining the possibility of in-phase and out-of-phase synchronization. As seen in Fig. 2.8, changing the mass ratio of the pendula to the center mass can lead to a transition between the synchronized states [1, 8, 10, 15]. The effect of pendulum natural frequency difference was also investigated, and the results are in agreement with Huygens' observations from 1665.

Chapter 3

Kicked Rotor

The kicked rotor is a well-known model in nonlinear dynamics. Among other things, it demonstrates the utility of using phase space when interpreting system behavior [27]. In recent years, the kicked rotor has been used in the field of quantum mechanics to model quantum chaos and dynamic localization from interference, (e.g., atoms standing in ultra-cold atomic gases and microwave fields) [27, 28]. The kicked rotor describes the motion of a particle rotating around a fixed point. The particle experiences a periodic excitation, the strength of which depends on its angular position. One can think of the excitation as a gravitational force that is applied in short periodic impulses which change the particle's angular velocity. In this chapter, the synchronization of two kicked rotors is of interest.

3.1 Hamiltonian Mechanics

A general knowledge of classical dynamics and the Kolmogorov-Arnold-Moser theory as it relates to phase space will improve the understanding of the forthcoming results. In the case of the kicked rotor, two state variables—angle and momentum—define its two dimensional phase space. As previously defined, the Hamiltonian represents the total energy in a system, i.e., the sum of the kinetic and potential energies, Eq. (2.11). In low-order systems, deciding whether to use Hamiltonian or Lagrangian is of little significance; however, the Hamiltonian is often preferred in the field of quantum mechanics where a large number of particles are of interest [29]. More importantly, using the Hamiltonian gives way to dynamic principles that allow for a better interpretation of systems in phase space. Rather than using position and velocity variables for defining the system equations, the Hamiltonian relies on position and momentum variables respectively.

To start, variable p_i is introduced as the conjugate momentum for a particle i with generalized coordinate q_i. Without getting into too much detail about the exact derivation of the Hamiltonian using the Legendre transformation, the Hamiltonian may be rewritten such that

$$\mathcal{H} = \left(\sum_{i=1}^{N} p_i \dot{q}_i \right) - \mathcal{L} \tag{3.1}$$

where the i^{th} momentum equals the partial of the Lagrangian with respect to velocity, $\dot{q}_i$

$$p_i = \frac{\partial \mathcal{L}}{\partial \dot{q}_i}. \tag{3.2}$$

Note that even though it might not look intuitive, Eq. (3.1) still represents the system's total energy. It should also become apparent that q and p represent a set canonical coordinates for the system that will dictate its motion through phase space [30]. To then find the according time dependent coordinates for position, $q_i(t)$, and momentum, $p_i(t)$, Hamilton's equations of motion become useful,

$$\frac{dq_i}{dt} = +\frac{\partial \mathcal{H}}{\partial p_i}, \quad \frac{dp_i}{dt} = -\frac{\partial \mathcal{H}}{\partial q_i}. \tag{3.3}$$

The coming section shows a derivation for this set of equations through Poisson brackets.

3.1.1 Integrability

Now that the Hamiltonian is more clearly defined, one may introduce the concept of integrability. Integrability attributes the regular evolution of Hamiltonian trajectories, thereby system states, in a defined phase space [31, 32]. It denotes that all Hamiltonian system states, for all time, may be characterized through defined sets of differential equations [30, 31]. To classify a system as integrable requires an understanding of a first integral, also known as a constant of motion. A function $f(q_i, p_i, t)$ in phase space represents a first integral if $\dot{f} = 0$ or equivalently $f(q(t), p(t), t) = \alpha$ where α equals an arbitrary constant, hence the name 'a constant of motion' [33]. Suppose an n-dimensional Hamiltonian system whose motion remains retained through some canonical transformation (q, p) $\rightarrow$ ($\overline{q}$, $\overline{p}$). If the system can be broken into n independent first integrals (f_1, f_2, ..., f_n) in involution of the canonical coordinates q and p then it is considered to be integrable [30–34]. This implies that the momentum of an integrable system equals a constant (i.e. $p_i = \alpha_i$). If on the other hand, these conditions are not preserved then initial conditions generate trajectories that diverge [32]. Though integrability is rarely preserved in real dynamic system, it forms a foundation for evaluating complex dynamic systems.

Alternatively, introducing Poisson brackets for a Hamiltonian system further helps to characterize the canonical coordinates and involution. By definition, the Poisson bracket (indicated by [,]) of two functions in terms of the canonical coordinates will vanish if they are in involution [35]. As an example, take a dynamic function $g(q, p, t)$ with n degrees of freedom where $q(t)$ and $p(t)$ provide the system state [31,35]. Here, using Eq. (3.3), the total change of g with time becomes

$$\frac{dg}{dt} = \frac{\partial g}{\partial t} + \sum_{i=1}^{n} \left(\frac{\partial g}{\partial q_i} \frac{dq_i}{dt} \right) + \sum_{i=1}^{n} \left(\frac{\partial g}{\partial p_i} \frac{dp_i}{dt} \right), \tag{3.4a}$$

$$\frac{dg}{dt} = \frac{\partial g}{\partial t} + \sum_{i=1}^{n} \left(\frac{\partial g}{\partial q_i} \frac{\partial \mathcal{H}}{\partial p_i} - \frac{\partial g}{\partial p_i} \frac{\partial \mathcal{H}}{\partial q_i} \right) \tag{3.4b}$$

$$\frac{dg}{dt} = \frac{\partial g}{\partial t} + [g, \mathcal{H}]. \tag{3.4c}$$

If g is no longer a function of time, i.e. $\frac{dg}{dt} = 0$, then $\frac{\partial g}{\partial t} = 0$ and therefore $[g, \mathcal{H}] = 0$. The function $g(q, p) = \alpha$, indicating constant motion. Following the same procedure as above, Eq. (3.4) for our generalized coordinate, $g = p_i$, or the conjugate momentum, $g = q_i$, provides

$$[q_i, \mathcal{H}] = \dot{q}_i = \frac{\partial \mathcal{H}}{dp_i}, \quad [p_i, \mathcal{H}] = \dot{p}_i = -\frac{\partial \mathcal{H}}{dq_i}, \tag{3.5}$$

i.e., the previously defined Hamilton's equation of motion, Eq. (3.3) [33]. Satisfying the following relation through Poisson brackets ensures that the canonical transformation remains,

$$[q_i, q_j] = [p_i, p_j] = 0, \quad [q_i, p_j] = \delta_{ij}. \tag{3.6}$$

Furthermore, the independence between q and p induces a symmetry in Eq. (3.5) which has been the origin of numerous principles in classical dynamics, such as Liouville's theorem [29]. As will be discussed, these properties give way to the formation of multi-dimensional phase space boundaries [30].

3.1.2 Phase Space Topology

For an integrable dynamic system with n degrees of freedom, there exists a manifold of dimension $2n$ (typically denoted by M) which encompasses all phase space trajectories of that system [30, 31, 33, 34]. In other words, the motion of a Hamiltonian system is bounded to a certain subspace primarily due to principles of conservation [31]. This means that the initial conditions of the system drive its subsequent motion and thereby define M [32]. One of the simplest topologies that permits such a region in phase space is that of

an n-dimensional torus. In classical dynamics, the name invariant tori refers to the idea that each trajectory remains bounded to the surface of that torus, see Fig. 3.1. Due to integrability, trajectories—and hence their tori— cannot intersect, which means each torus corresponds to a unique set of initial conditions [31]. Taking the action integral of a Hamiltonian trajectory over a single period presents the action variable, J_k,

$$J_k = \frac{1}{2\pi} \oint p_k dq_k. \tag{3.7}$$

The action variables geometrically define the surface of the invariant torus and become essential when introducing the idea of perturbations. It should also be noted that based on the canonical transformation for an integrable, time-invariant system, J is constant [32, 36]. Through what are called angle coordinates, one can then specify the exact location of a system's trajectory on that torus [30, 31, 33]. Writing the angle coordinates with time and angular frequency would look as follows [31],

$$\theta_i(t) = \omega_i t + \beta_i. \tag{3.8}$$

such that $\beta_i = \theta_i(0)$ for i=1, ..., n [31].

Using Fig. 3.1 as a reference, if the ratio of the angular frequencies, ω_1 and ω_2, for $\theta_1(t)$ and $\theta_2(t)$ respectively, equals a rational number then the trajectory will connect back onto itself (i.e $\omega_1/\omega_1 = l$, where l equals a rational number). From this periodicity we classify the torus as a resonant torus which means that the trajectory will never fully engulf the surface of the torus. Alternatively when looking at the Poincaré section of a non-resonant torus, or a quasiperiod system, then the enclosed 2-dimensional contour would be fully covered.

Isolating a transverse plane of the a torus reveals the system's Poincaré section where points are marked each time that a trajectory intersects the plane. This allows us to collapse system dimensions while still observing characteristics in the system's behavior. Fig. 3.1 shows how a Poincaré section fits into the phase space with a two dimensional torus. Here, the points on the plane show what would be seen on a Poincaré section for these three time dependent, periodic trajectories.

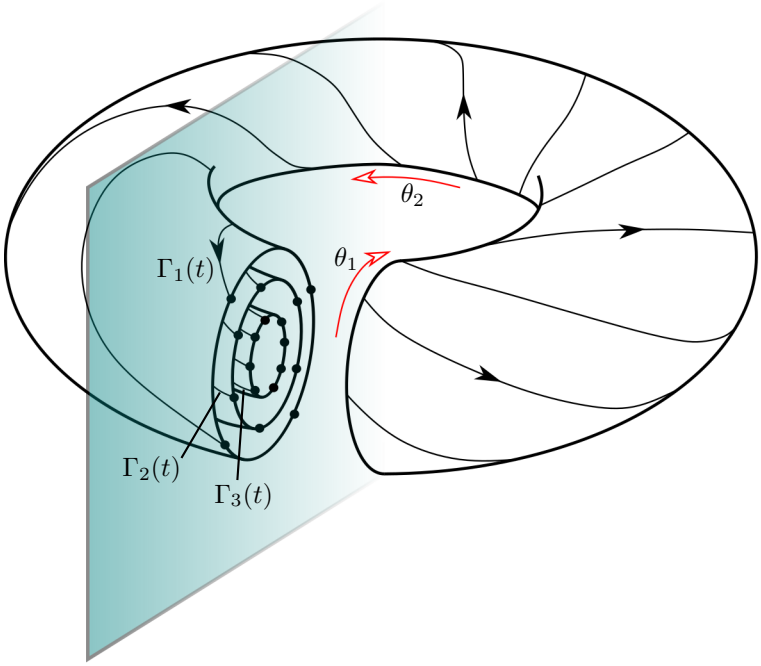

Figure 3.1. Visualization of 3 2-dimensional invariant tori and their cross-section with a 4-dimensional phase space. Here, $\Gamma_1(t)$, $\Gamma_2(t)$ and $\Gamma_3(t)$ correspond to 3 time dependent separate trajectories, or 3 separate system initial conditions. As seen, the location of the outer trajectory, $\Gamma_3(t)$, can be fully specified through the angle coordinates, θ_1, θ_2. The figure was adapted from Refs. [30, 31]

3.2 Kolmogorov-Arnold-Moser Theorem

A big motivator of classical mechanics originated from the desires of mathematicians and physicists to explain planetary motion [30]. At one point, it was believed that planetary orbits mirror the dynamic trajectories of integrable systems in phase space as seen on the surface of an invariant torus, Fig. 3.1. However, due to perturbations, orbits always diverged onto alternative paths. It wasn't until 1954 when Andrey Kolmogorov discovered a new theory, bridging perturbations to principles of classical mechanics [30, 31]. Known as Kolmogorov-Arnold-Moser (KAM) theory, it considers the motion of Hamiltonian dynamical systems and their resilience under perturbations to maintain phase space trajectories [30, 31]. At the time, this was a huge breakthrough as invariant tori managed to survive certain perturbations [30]. These deformed tori, known as KAM tori, restrict stochastic trajectories, forming boundaries for different initial

condition sets [34]. In other words, the system embodies a combination of an integrable Hamiltonian, $\mathcal{H}_0$, in addition to a perturbation function ,$\mathcal{H}_1$,

$$\mathcal{H}(J_1, ..., J_n, \theta_1, ..., \theta_n) = \mathcal{H}_0(J_1, ..., J_n) + \epsilon\mathcal{H}_1(J_1, ..., J_n, \theta_1, ..., \theta_n). \tag{3.9}$$

Hence, systems that embody this behavior are also known as near-integrable. Here, the magnitude of ϵ determines the scale of the perturbations. At a certain critical value of ϵ, some trajectories will no longer retain the topology of deformed tori but rather diffuse into phase space. The outcome of the trajectory originates with the initial conditions. Those trajectories that do resemble deformed tori actually create boundaries, also known as KAM boundaries, in phase space that act as barrier for stochastic trajectories [30]. Figs. 3.2 and 3.3 in the coming section, Sec. 3.3, will provide a visualization of the covered concepts.

3.3 Classical Kicked Rotor

After covering the key fundamentals of classical dynamics features of the Poincaré section of a kicked rotor can be correlated to the global motion of the system. To start, the Hamiltonian for the system will be shown. The 1-dimensional system uses θ for its generalized coordinate. The Lagrangian then simply becomes the kinetic energy of the rotor minus the potential energy due to an arbitrary, pulsed gravitational field, g,

$$\mathcal{L} = \frac{1}{2}m\ell^2\dot{\theta}^2 - mg\ell\cos\theta. \tag{3.10}$$

Plugging the Lagrangian into the momentum equation, Eq. (3.2), yields

$$p = \frac{\partial\mathcal{L}}{\partial\dot{\theta}} = m\ell^2\dot{\theta}. \tag{3.11}$$

Next, using both Eqs. (3.10) and (3.11) in Eq. (3.1) gives us the Hamiltonian, $\mathcal{H}(p, q)$, of the rotor with a pulsed potential field that is proportional to constant K,

$$\begin{aligned}\mathcal{H} &= \frac{p^2}{2m\ell^2} + mg\ell\cos\theta \\ &= \frac{p^2}{2I} + K\cos\theta \\ &= \frac{p^2}{2I} + K\cos\theta\sum_{n=-\infty}^{\infty}\delta(t - nT)\end{aligned} \tag{3.12}$$

where $I = m\ell^2$, $K = mg\ell$ and δ, the Dirac delta function or impulse function [34, 37]. Hence, at times $t = 0, \pm T, \pm 2T, ..., \pm nT$, the rotor receives the 'kick' [37]. To further break down the system, Hamilton's equations of motion, Eq. 3.3, are useful for defining the kicked rotor in phase space.

$$\frac{d\theta}{dt} = +\frac{\partial \mathcal{H}}{\partial p} = \frac{p}{I} \tag{3.13a}$$

$$\frac{dp}{dt} = -\frac{\partial \mathcal{H}}{\partial \theta} = K \sin\theta \sum_{n=-\infty}^{\infty} \delta(t - nT) \tag{3.13b}$$

Plotting the state variables at each period gives way to the Poincaré section. To compensate for system periodicity and momentum dependence on theta, taking a modulo of 2π of both θ and p values will help retain system bounds. The system equations can be further simplified so that the variables, θ and p, are only captured at each period for the Poincaré section [37],

$$\theta_{n+1} = \theta_n + \frac{T}{I} p_{n+1}, \quad p_{n+1} = p_n + \frac{T}{I} K \sin\theta_n. \tag{3.14}$$

To non-dimensionalize the variables as in Ref. [37], $\frac{T}{I} p_{n+1} \to p_n$ and $\frac{T}{I} K \to K$, such that

$$\theta_{n+1} = \theta_n + p_{n+1}, \quad p_{n+1} = p_n + K \sin\theta_n. \tag{3.15}$$

Fig. 3.2 shows the well known transition from KAM trajectories to complete chaotic behavior for four different values of K (K=0.5, 0.97, 2.0 and 7.0). Here, each color in the Poincaré section presents a different set of initial conditions, and therefore its own phase space trajectory. As mentioned, in the case of near-integrable systems, trajectories will fully clutter the surface of their KAM tori and appear as deformed ellipses in the Poincaré section. When $K = 0.5$, Fig. 3.2a, cross sections of these KAM tori are clearly identifiable. However, as K moves up to 0.97, one starts to see the destruction of some of these trajectories. Similar to ϵ in Eq. (3.9), K has a critical value at which trajectories abandon their tori. The critical value at which all KAM trajectories cease to appear is $K_c \approx 0.9716$ [32, 34, 37, 38]. At values $K > K_c$, the rotor experiences substantial perturbations, making its corresponding phase change appear stochastic [32, 38]. When $K = 2.0$, Fig. 3.2c, the phase plot is almost completely characterized by stochasticity with only very few, heavily deformed KAM tori remaining. Increasing K up 10.0, as in Fig. 3.2d, globally diffuses all trajectories into the phase space. At this point the Poincaré section no longer suggests any form of ordered behavior.

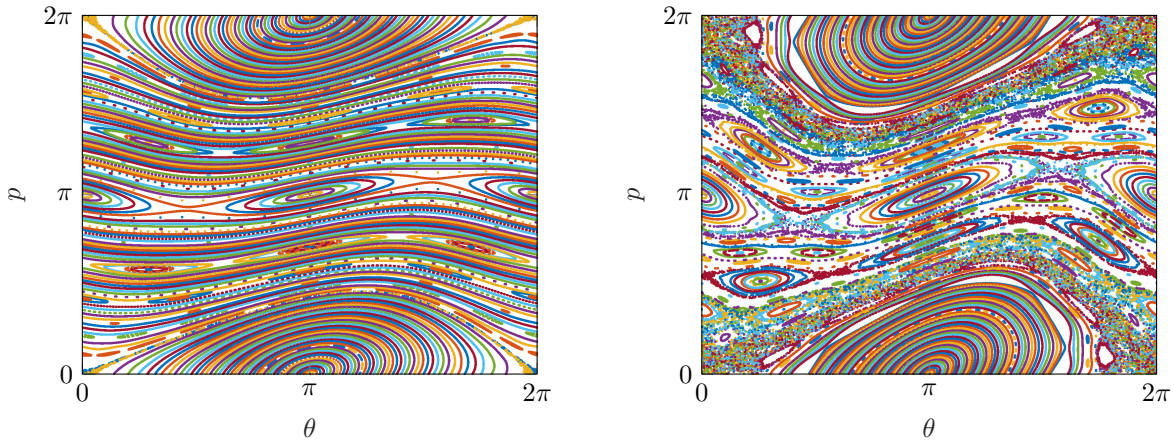

(a) $K = 0.5$

(b) $K = 0.97$

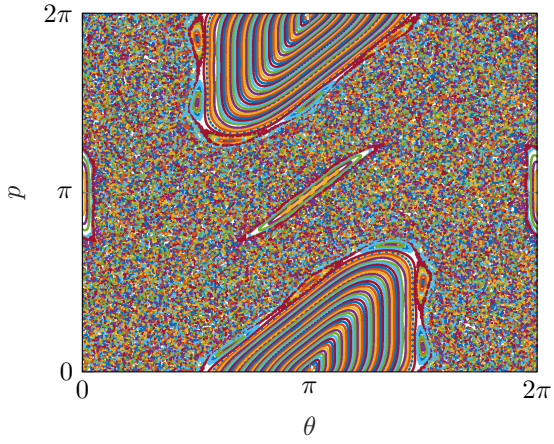

(c) $K = 2.0$

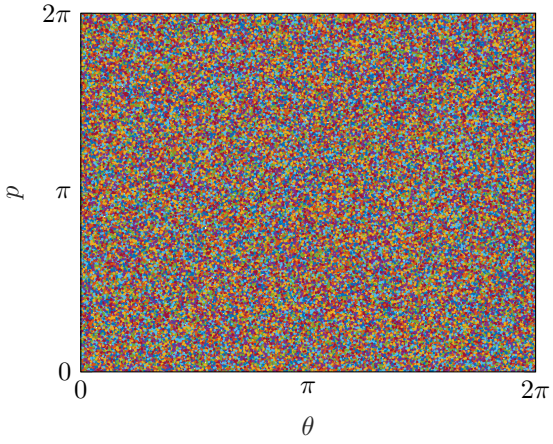

(d) $K = 10.0$

Figure 3.2. Poincaré sections of the kicked rotor for K values varying from 0.5, 0.97, 2.0, to 10.0. Each individual plot contains 200 trajectories for varying initial momenta, p_0, over 1000 periods, such that $p_0 = \frac{2\pi i}{N_{trajectory}}$ while $\theta_0 = \pi$.

Fig. 3.3 is a follow-on on Fig. 3.2 in that it shows the effect of varying the initial angle, θ_0, rather than K. Here, the K values stay fixed at 0.97 while p_0 incrementally adjusts between trajectories. As the initial angle shifts from 0 to π, trajectories start to branch over preexisting KAM boundaries to engulf vacancies in phase space. However, between all four plots, the general typologies remain alike in that areas with stochastic trajectories continue to consume the same specific regions.

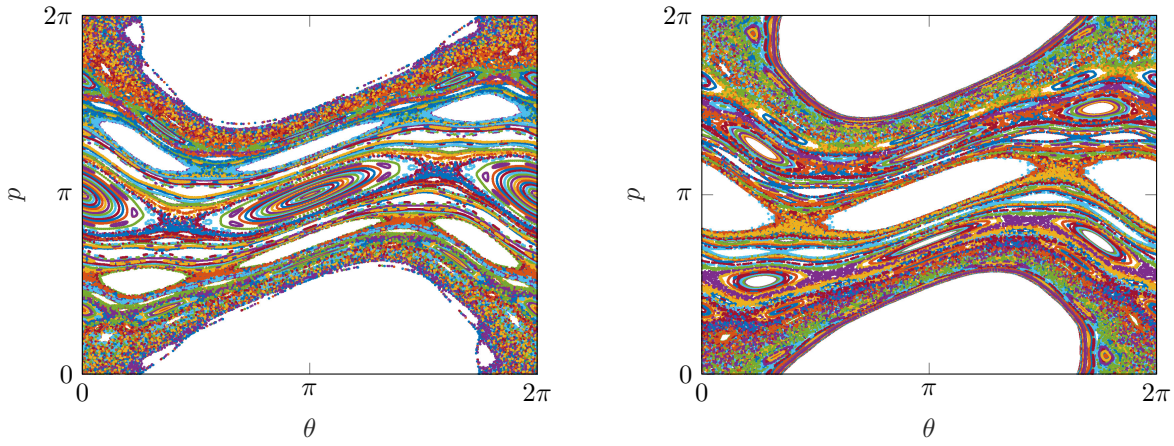

(a) $\theta_0 = 0$

(b) $\theta_0 = \frac{\pi}{3}$

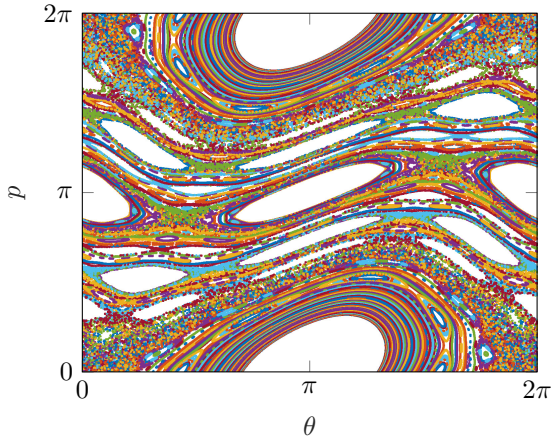

(c) $\theta_0 = \frac{2\pi}{3}$

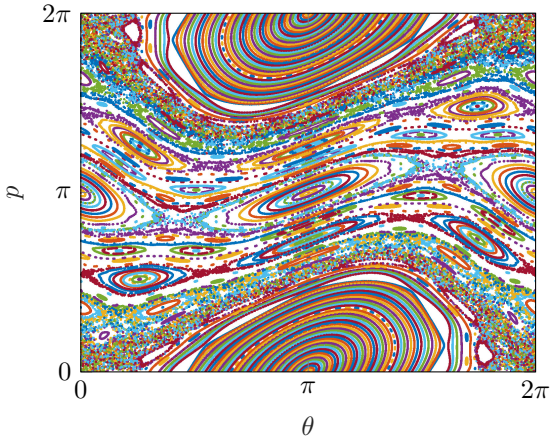

(d) $\theta_0 = \pi$

Figure 3.3. Poincaré sections of the kicked rotor for θ_0 values varying from 0, $\frac{\pi}{3}$, $\frac{2\pi}{3}$, to π with K fixed at 0.97. Again, each Poincaré section contains 200 combinations for the initial momentum, p_0, using the same algorithm as Fig. 3.2.

3.4 Two Kicked Rotors Sharing a Common Momentum

Here the motion of two identical kicked rotors is considered. In the Huygens' clock model, a rigid mass connected the two pendula, which ultimately allowed them to synchronize. Rather than using a rigid body to physically couple the rotors, the rotors are coupled by assigning the momentum of one rotor to the other.

The motion of the primary rotor is again found using Eq. (3.1) and Eq. (3.3), while the state of the second rotor incorporates is found using,

$$\theta_{2,n+1} = \theta_{2,n} + p_{2,n+1}, \quad p_{2,n+1} = p_{1,n} + K \sin \theta_{2,n} \tag{3.16}$$

where $p_{1,n}$ represents the primary rotor's momentum for the current period, n. As may be logically surmised, this adaptation does not allow for persisting out-of-phase synchronization.

After some transient period, the motion of each rotor may be either periodic or chaotic. To classify the post-transient motion as periodic or chaotic, a heuristic approach is used. First, the rotors' response is expressed in the frequency domain using an FFT. In the frequency domain, periodic motion is characterized by narrow, discrete peaks, while chaos is characterized by a broadband spectrum. Next, an amplitude threshold is set and the number of peaks crossing that threshold are counted. If the number of exceedances is large, the spectrum is broadband and the response is assumed to be chaotic. Alternatively, if the number of exceedances is relatively low, the response is assumed to be periodic [39]. Representative chaotic and periodic frequency spectra are shown in Fig. 3.4, and the distinction between a periodic and chaotic responses is quite apparent. The dashed red line indicates the threshold line. For this study, the response is considered chaotic if more than 200 values fall above shown threshold line, which set at 5×10^{-3}.

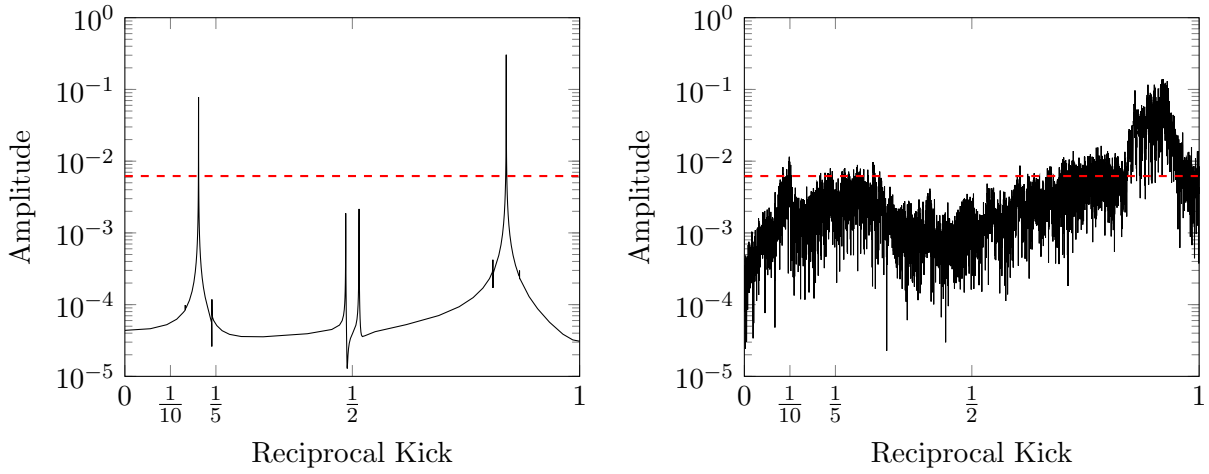

(a) Periodic response of the kicked Rotor

(b) Chaotic response of the kicked Rotor

Figure 3.4. Example of (a) periodic and (b) chaotic response of the kicked rotor in the frequency domain. The dashed line indicates the threshold for categorizing the response according to how many points fall above it.

Given a set of initial conditions, the response of the two rotors can be categorized by the following six post-transient states:

(1) periodic synchronization

(2) chaotic synchronization

(3) no synchronization, periodicity in primary rotor and chaos in secondary rotor

(4) no synchronization, chaos in primary rotor and periodicity in secondary rotor

(5) no synchronization and chaos in both

(6) no synchronization and periodicity in both

Fig. 3.5 maps these six states across a range of initial conditions. The maps consider half a million initial angle coordinates ranging from 0 to 2π, where the color represents the system state after the 1,000$^{\text{th}}$ kick. Fig. 3.5a shows that for low K values, only two different system states exist—-periodic synchronous motion and periodic asynchronous motion. Low K values represent near integrable systems with clearly identifiable KAM tori, so the periodic responses are to be expected. As K increases to one, sections of synchronized chaos make an appearance, identifiable by the vertical orange columns. Here, all chaotic behavior is synchronous. Increasing K to 1.25 expands the regions of synchronous chaos. It is not until $K = 1.5$, that asynchronous chaos can be observed (dark blue). This behavior can be found intermingled with synchronous chaos behavior. At $K = 2$, no synchronous motion is found. Note that for moderate to high values of K, the response is largely insensitive to the initial angle of the second rotor.

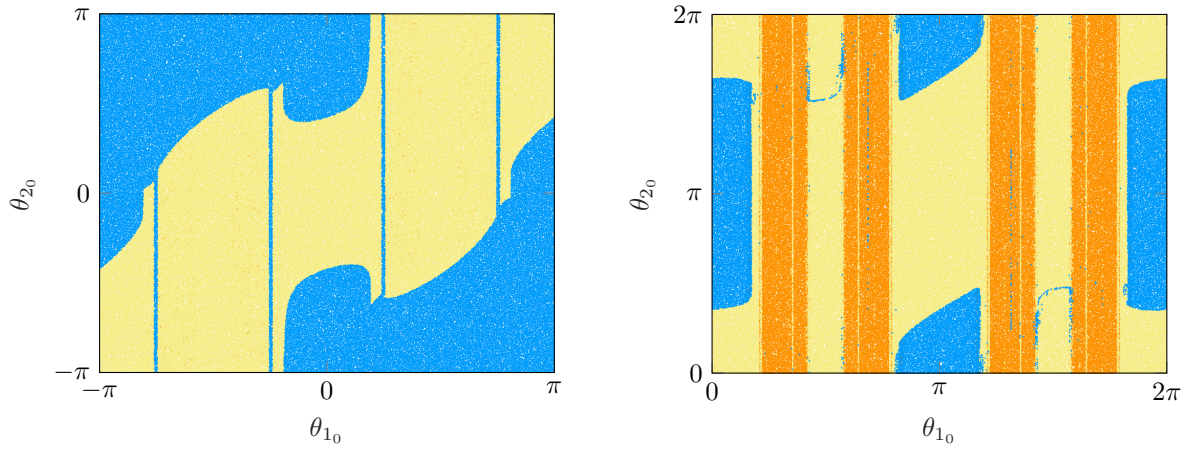

(a) K=0.1

(b) K=1

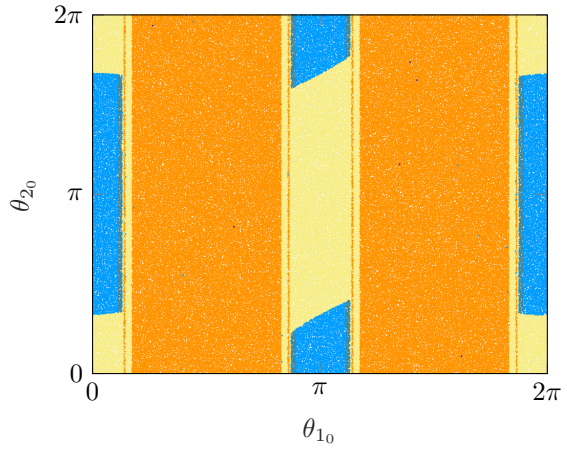

(c) K=1.25

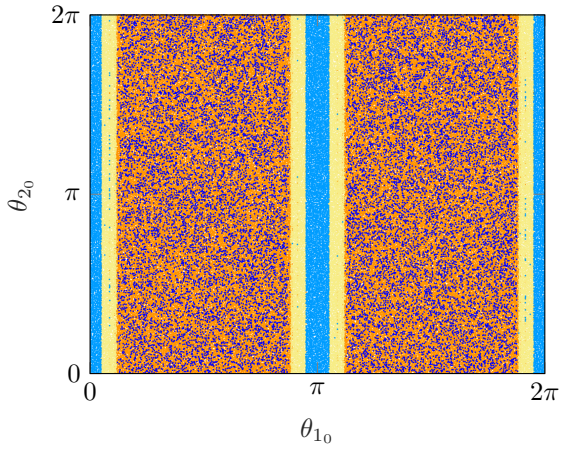

(d) K=1.5

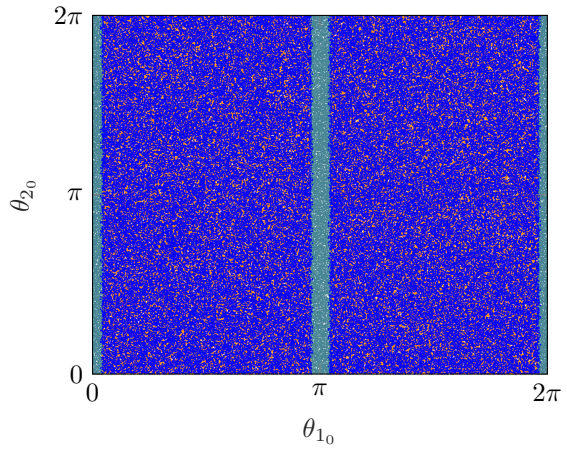

(e) K=2

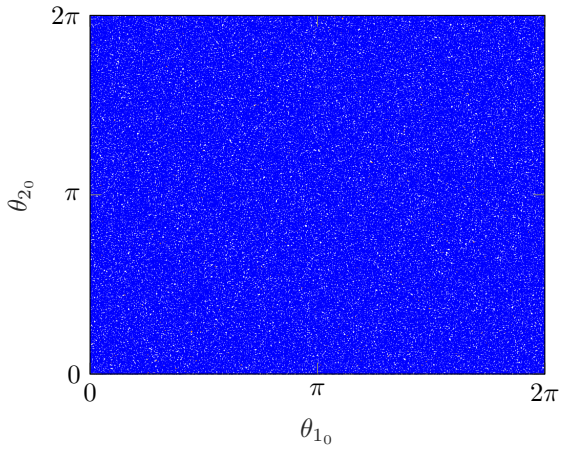

(f) K=5

Figure 3.5. Initial conditions maps for various values of K. The initial momentum of the primary rotor, p_{1_0}, is fixed at π. Each color represents one of the six post transient states as described in the text.

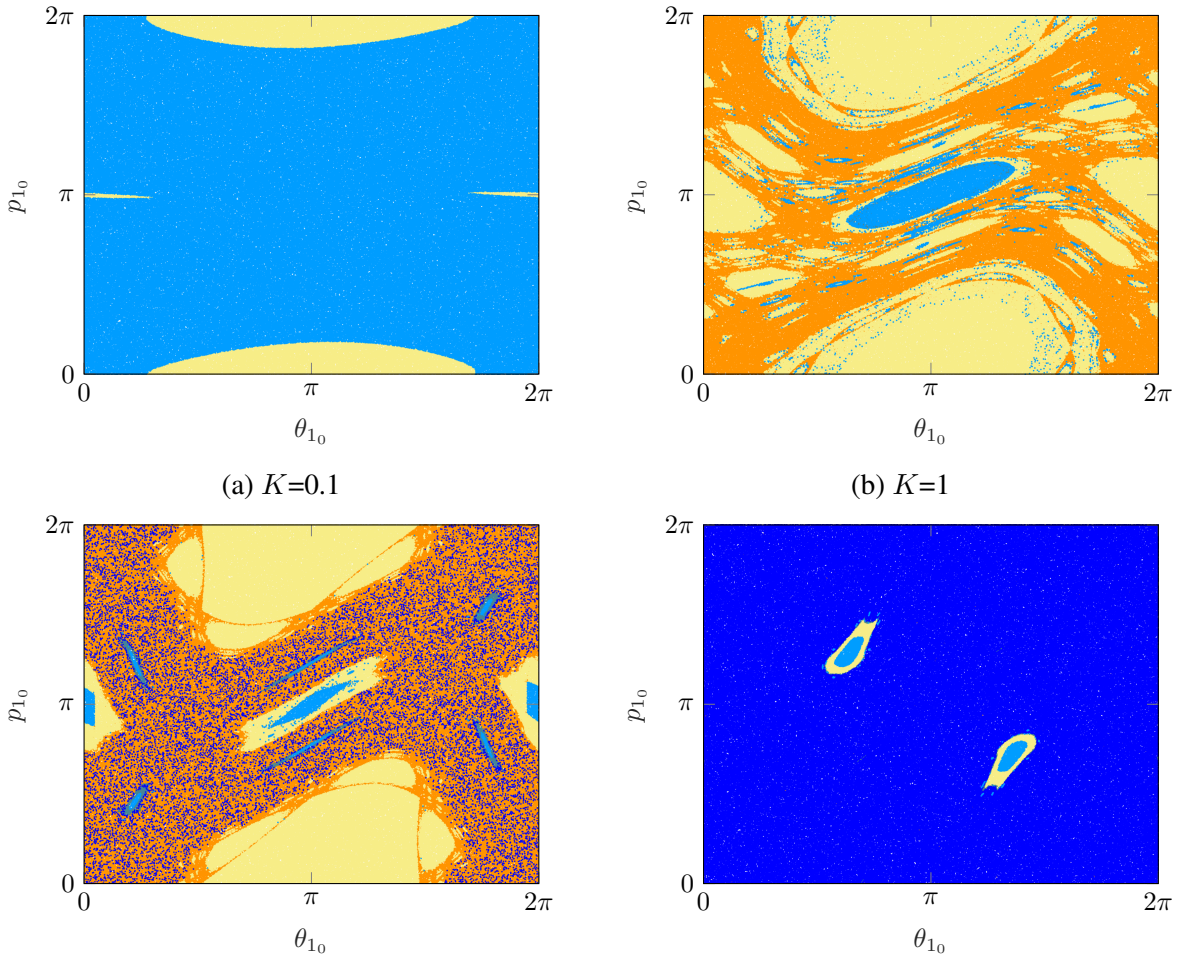

(a) K=0.1

(b) K=1

(c) K=1.5

(d) K=5

Figure 3.6. Initial conditions maps that again vary by K. The initial angle, θ_{2_0}, of the second rotor is fixed at π. The colors associated with the six post-transient states are described in the text.

3.5 Summary

Here, it was shown that two kicked rotors are capable of exhibiting both chaotic and periodic synchronization provided the momentum of one rotor is passed to the other. This type of synchronization can be classified as controlled. The model is attractive because it can demonstrate synchronized chaos using a standard iterative map, i.e., the numerical integration of nonlinear ODEs is not necessary.

Chapter 4

Future Work

While the Huygens' clocks model has been explored rather extensively, there a many unexplored aspects of the dual kicked rotor model. The classical kicked rotor is an excellent platform for studying quantum mechanics [30–32, 34, 37, 38]. Introducing quantum modifications in the kicked rotor creates an adaptation known as the quantum kicked rotor. This model has found numerous applications relating to the Bose-Einstein condensate (BEC), including atom optics and currents, as well as the diffusion of waves in the atomic lattice [27, 28, 40, 41].

For future work, it would be interesting to perform a quantum modification of the dual coupled kicked rotor model to check for further analogies in the quantum realm. There have already been discussions on quantum non-locality from synchronized chaos [42]. Quantum non-locality is the basis of the Einstein, Podolsky and Rosen Paradox which claims the incompleteness of quantum mechanic [43], i.e. "Can Quantum-Mechanical Description of Physical Reality Be Considered Complete?" The paradox arises when looking at the position and momenta of two entangled particles according to quantum mechanics. In entangled particles, the state of one particle is partially dependent on that of the other. By principles of locality, for two distant entangled particles to interact requires some type of interface, for example a wave or additional particle [44]. This relates to the idea that interfaces between oscillators are a necessity for synchronization (see Sec. 1.1). Here is the reason for the paradox: as soon as the state of the first entangled particle is measured, either through position or momentum, the respective position or momentum of the second particle is simultaneously known [44, 45]. In other words, information between the two entangled particles exchanges faster than the speed of light, contradicting Einstein's Theory of Relativity. Hence, the argument for an incompleteness of quantum mechanics was made [43]. Since a single rotor has been a widely used tool for

studying behaviors in quantum mechanics, novel adaptations of the dual rotor system may prove useful.

The dual kicked rotor model could be further modified by changing the interface between the kicked rotors, perhaps by introducing a rigid body, as in the Huygens' clock model. The two rotors could then interact passively. However, initial investigations with this passive coupling showed that there are no initial condition sets under which such a model synchronizes. The synchronization of the present system can be classified as controlled, thus self-synchronization of a dual kicked rotors has yet to be shown.

Bibliography

[1] Peña, J. (2013). *Huygens' synchronization of dynamical systems : beyond pendulum clocks*. Eindhoven: Technische Universiteit Eindhoven. doi: 10.6100/IR748516

[2] Jovanovic, V., and Koshkin, S. (2012). *Synchronization of Huygens' clocks and the Poincaré method*. Journal of Sound and Vibration, 331(12), 2887–2900. https://doi.org/10.1016/j.jsv.2012.01.035

[3] Xi, K., Dubbeldam, J. L., and Lin, H. X. (2017). *Synchronization of Cyclic power grids: Equilibria and stability of the Synchronous state*. Chaos: An Interdisciplinary Journal of Nonlinear Science, 27(1), 013109. doi:10.1063/1.4973770

[4] Nijmeijer, H., and Rodriguez-Angeles, A. (2003). *Synchronization of mechanical systems*. World Scientific Series on Nonlinear Science Series A. doi:10.1142/5391

[5] Blekhman, I., Fradkov, A., Nijmeijer, H., and Pogromsky, A. (1997). *On self-synchronization and controlled synchronization*. Systems and Control Letters, 31(5), 299-305. doi:10.1016/s0167-6911(97)00047-9

[6] Dictionary by Merriam-Webster: America's most-trusted online dictionary. (1986). Retrieved October 21, 2020, from https://www.merriam-webster.com/

[7] Kerschen, G., Peeters, M., Golinval, J., and Vakakis, A. (2009). *Nonlinear normal modes, part I: A useful framework for the structural dynamicist*. Mechanical Systems and Signal Processing, 23(1), 170-194. doi:10.1016/j.ymssp.2008.04.002

[8] Willms, A. R., Kitanov, P. M., and Langford, W. F. (2017). *Huygens' Clocks Revisited*. The Royal Society. doi: 10.1098/rsos.170777

[9] Mahoney, M., *Christian Huygens: The Measurement of Time and of Longitude at Sea, in Studies on Christiaan Huygens*, ed. H.J.M. Bos et al. (Lisse: Swets, 1980), 234-270.

[10] Ramirez, J. P., Olvera, L. A., Nijmeijer, H., and Alvarez, J. (2016). *The Sympathy of Two Pendulum Clocks: Beyond Huygens' Observations*. Scientific Reports, 6(1). doi:10.1038/srep23580

[11] Huygens, C. (1966). *Horologium oscillatorium*. London, Dawsons of Pall Mall.

[12] Blekhman, I.I., *Sinkhronizatsiya dinamicheskikh sistem (Synchronization of Dynamical Systems)*, Moscow: Nauka, 1971

[13] Fradkov, A. L. (2007). *Cybernetical physics: From control of chaos to quantum control*. Berlin, Germany: Springer.

[14] Bennett, M., Schatz, M. F., Rockwood, H., and Wiesenfeld, K. (2002). *Huygens's Clocks*. Proceedings of the Royal Society of London. Series A: Mathematical, Physical and Engineering Sciences, 458(2019), 563-579. doi:10.1098/rspa.2001.0888

[15] Pantaleone, J. (2002). *Synchronization of metronomes. American Journal of Physics*, 70(10), 992-1000. doi:10.1119/1.1501118

[16] Arenas, A., Díaz-Guilera, A., Kurths, J., Moreno, Y., and Zhou, C. (2008). *Synchronization in complex networks*. Physics Reports, 469(3), 93-153. doi:10.1016/j.physrep.2008.09.002

[17] Eroglu, D., Lamb, J. S., and Pereira, T. (2017). *Synchronization of chaos and its applications*. Contemporary Physics, 58(3), 207-243. doi:10.1080/00107514.2017.1345844

[18] Schmidt, R. (2016). *Wristwatch Handbook - A Comprehensive Guide to Mechanical Wristwatches*. Acc Art Books.

[19] *Prix Gaïa 2009 – Beat Haldimann. Craftsmanship-Creation Category* (2009, September 20). Retrieved September 20, 2020, from https://www.watchonista.com/articles/history/prix-gaia-2009-beat-haldimann-craftsmanship-creation-category

[20] Fradkov, A. L., and Pogromsky, A. Y. (1998). *Introduction to Control of Oscillations and Chaos. World Scientific Series on Nonlinear Science Series A*. doi:10.1142/3412

[21] Acosta, J., Gordillo, F., and Aracil, J. (2001). *A New SG Law for Swinging the Furuta Pendulum Up*. IFAC Proceedings Volumes, 34(6), 795-800. doi:10.1016/s1474-6670(17)35276-x

[22] Seifullaev, R. E. (2012). *Speed Gradient Energy and Sampled-Data Control of Cart-Pendulum System*. IFAC Proceedings Volumes, 45(11), 478-483. doi:10.3182/20120619-3-ru-2024.00079

[23] Malham, S. J. (2015). *An introduction to Lagrangian and Hamiltonian mechanics*. doi:10.13140/RG.2.1.2914.8003

[24] Andrievsky, B. R. (2011). *Global stabilization of the unstable Reaction-Wheel Pendulum. Automation and Remote Control*, 72(9), 1981-1993. doi:10.1134/s0005117911090189

[25] Controlled synchronization of pendula. (2003). Controlled synchronization of pendula. *Proceedings of the 42nd IEEE Conference on Decision and Control*. Maui, Hawaii USA

[26] Blekhman, I., Fradkov, A., Tomchina, O., and Bogdanov, D. (2002). *Self-synchronization and controlled synchronization: General definition and example design*. Mathematics and Computers in Simulation, 58(4-6), 367-384. doi:10.1016/s0378-4754(01)00378-0

[27] Korsch, H. J., Graefe, E. M., and Jodl, H. (2008). *The kicked rotor: Computer-based studies of chaotic dynamics*. American Journal of Physics, 76(4), 498-503. doi:10.1119/1.2870327

[28] Qin, P., Andreanov, A., Park, H. C., and Flach, S. (2017). *Interacting ultracold atomic kicked rotors: Loss of dynamical localization*. Scientific Reports, 7(1). doi:10.1038/srep41139

[29] Morin, D. J. (2007). *Introduction to classical mechanics: With problems and solutions*. In Introduction to classical mechanics: With problems and solutions (pp. XV-1-XV-15). Cambridge: Cambridge University Press.

[30] Dumas, H. S. (2014). *The KAM story: A friendly introduction to the content, history, and significance of classical Kolmogorov-Arnold-Moser theory*. Hackensack, NJ: World Scientific.

[31] Masoliver, J., and Ros, A. (2011). *Integrability and chaos: The Classical uncertainty*. European Journal of Physics, 32(2), 431-458. doi:10.1088/0143-0807/32/2/016

[32] Lichtenberg, A. J., and Lieberman, M. A. (1992). *Regular and chaotic dynamics*. Applied Mathematical Sciences. doi:10.1007/978-1-4757-2184-3

[33] Dunajski, M. (2015). *Solitons, instantons, and twistors*. Oxford, NY: Oxford University Press.

[34] Daley, A. J., Parkins, A. S., Leonhardt, R., and Tan, S. M. (2002). *Diffusion resonances in action space for an atom optics kicked rotor with decoherence*. Physical Review E, 65(3). doi:10.1103/physreve.65.035201

[35] Scheck, F. (1990). *Mechanics: From Newton's laws to deterministic chaos*. Berlin: Springer.

[36] Steward, I. (2016). *Mechanics: Advanced Classical Mechanics*. Massachusetts Institute of Technology: MIT OpenCouseWare, https://ocw.mit.edu/. License: Creative Commons BY-NC-SA.

[37] Bender, C. M., Feinberg, J., Hook, D. W., and Weir, D. J. (2009). *Chaotic systems in complex phase space*. Pramana, 73(3), 453-470. doi:10.1007/s12043-009-0099-3

[38] Fishman, S., Grempel, D. R., and Prange, R. E. (1987). *Temporal crossover from classical to quantal behavior near dynamical critical points*. Physical Review A, 36(1), 289-305. doi:10.1103/physreva.36.289

[39] Wiebe, R., and; Virgin, L. N. (2012). *A heuristic method for identifying chaos from frequency content*. Chaos: An Interdisciplinary Journal of Nonlinear Science, 22(1), 013136. doi:10.1063/1.3675624

[40] Ni, J., Dadras, S., Lam, W. K., Shrestha, R. K., Sadgrove, M., Wimberger, S., and Summy, G. S. (2017). *Hamiltonian ratchets with Ultra-cold Atoms*. Annalen Der Physik, 529(8), 1600335. doi:10.1002/andp.201600335

[41] Sadgrove, M., and Wimberger, S. (2011). *A pseudoclassical method for the atom-optics kicked rotor*. Advances In Atomic, Molecular, and Optical Physics, 315-369. doi:10.1016/b978-0-12-385508-4.00007-3

[42] Duane, G. S. (2005). *Quantum Nonlocality From Synchronized Chaos*. International Journal of Theoretical Physics, 44(11), 1917-1931. doi:10.1007/s10773-005-8957-3

[43] Einstein, A., Podolsky, B., and Rosen, N. (1935). *Can quantum-mechanical description of physical reality be considered complete? Physical Review*, 47(10), 777-780. doi:10.1103/physrev.47.777

[44] Mittelstaedt, P. (2000). *The problem of decoherence and the EPR-Paradox*. Decoherence: Theoretical, Experimental, and Conceptual Problems, 149-159. doi:10.1007/3-540-46657-6_12

[45] Cantrell, C., and Scully, M. O. (1978). *The EPR Paradox Revisited*. Physics Reports, 43(13), 499-508. doi:10.1016/0370-1573(78)90211-9